SAND2019-6368B

Modeling of AlGaN/GaN pH Sensors

Authors: Madeline Esposito[1,2], Erin Patrick[2], Mark E. Law[2]
Affiliations: [1]Sandia National Laboratories, [2]University of Florida Electrical and Computer Engineering

Outline:

Introduction

While GaN-based devices have gained much attention for high power and high frequency applications, they are also attractive as sensors given its high sensitivity due to its high electron mobility. HEMT sensors have a fast response time and are currently the cheapest technology available for sensing [1]. The main design difference between the GaN-based HEMT technology for sensing applications versus its well-known high power and high frequency applications is leaving the gate area un-metalized and “open” to allow ions to interact with the surface. The sensing capability originates from measuring changes in the drain current resulting from the charged ions interacting at the surface, or open gate, of this device. Given GaN’s inertness to etching, nontoxicity, and wide-band gap, it is an ideal candidate for sensing in harsh environments; ranging from in vivo applications to radiation-hard sensors.

The need for inexpensive and reliable diagnostic testing is apparent with approximately 160,000 cases of prostate cancer [2] and 180,000 cases of breast cancer each year in the United States alone. Human exhaled breath condensate (EBC) has been shown to be a reliable detector of human pH [3]–[8] where human pH is a strong indicator of metabolic state and can indicate various forms of cancer [9]–[11], kidney injury [12], and glucose issues such as diabetes [9]. The human pH can range from 5 to 8, where a typical healthy human pH is between 7 and 8 [13]. Measuring pH can also be used to detect various drugs and medications which is valuable in measuring medication tolerance and reliability [1] . Accurate measurement of human pH through EBC can effectively replace uncomfortable, expensive, and time-consuming blood and urine tests.

The need for computational optimization emanates from lack of a general study of AlGaN/GaN HEMT device limitations in experimental literature. Simulation facilitates exploration of the device’s full range and identifies device parameters that result in maximal performance. Testing these aspects of the GaN-based HEMT chemical sensors

through simulation reduces testing time and cost, furthering future development of commercializing these devices in the biosensor market. This work builds upon a simple fundamental model of biological and chemical sensing of GaN-based High Electron Mobility Transistor (HEMT) and incorporates specific adsorption with the theory of an electrical double layer (EDL).

Background

1. Experimental Review

The interest in GaN-based devices evolved due to its unique ability to serve applications of radiation hardness [14]. The investigation began with gas sensors where GaN and SiC were known to be sensitive to a number of gases [14]. There was much activity in studying GaN-based transistors for gas sensing [15]–[25] where its success lead to the idea of sensing chemicals in electrolyte rather than gas [14]. Thus far, only 14 experimental studies have been conducted of these pH sensing GaN-based HEMTs with little variation of device and material parameters. These experiments are done case by case and collectively provide very little comprehensive understanding for optimal device operating conditions. Because this field is novel, there is much to investigate and comparatively limited literature to review.

In 2003, Steinhoff et al. pioneered the application of GaN-based transistors for pH. Sensing [23] as an alternative to Si-based ion-sensitive field effect transistors (ISFETs) [24], [25] due to its oxide layer, SiO_2, producing a low sensor response and poor sensor stability. Prior to Steinhoff et al., some work on III-nitride-based chemical sensors was done however the ion sensitivity of GaN surfaces in aqueous solutions was not systematically investigated [26], [27]. Steinhoff et al. studied the electrical response of deposited and thermally grown oxide GaN surfaces to variations of hydrogen ion, H^+, concentrations in electrolyte solutions [23]. This study measured the chemical response of the gate surface to changes in the electrolyte composition through adjusting a commonly used Ag/AgCl reference electrode to compensate for the ion-induced changes in the channel or drain current at a constant applied drain bias. Since this work there have been proof of concept studies [1], [9], [28]–[39] with this device for pH sensing while only testing a few parameters at a time and all with varied parameters (mobility, gate dimensions, AlGaN thickness/molarity, varied GaN oxide, etc), making it nearly impossible to observe trends for optimization.

Sensitivity is the standard metric to compare the response for these chemical sensors. Steinhoff et al. was the first to report a linear behavior with pH for this device with sensitivities (57.3 mV/pH for GaN:Si/GaN:Mg and 56.0 mV/pH for GaN/AlGaN/GaN HEMT) close to the Nernstian response to H^+ ions [23]. These sensitivities reported a drain current decrease with increasing pH. The Nernst equation is the theoretical value of the potential change with pH and is expressed in equation 1 [40] where k is Boltzmann's constant, T is temperature, and q is electron charge.

$$\psi_0 = -2.303\frac{kT}{q}\Delta pH \qquad 1$$

This equation may be regarded as a modified version of the Nernst equation relating potential, φ_0, to a change in pH, ΔpH [40], where at room temperature, 25°C, the equation is simplified to equation 2.

$$\psi_0 = -0.0589\Delta\text{pH} = -58.9\ \frac{\text{mV}}{\text{pH}} \qquad 2$$

However, transistor output is not commonly a unit of potential, but rather one of current. Sensor response is measured through a change in drain, or channel, current per change in pH (mA-mm/pH). These current based sensitivity values vary experimentally as there is no known theoretical value based on output current or even a correlation between output current and the Nernst equation for these devices. It is an accepted notion that improving the sensitivity is the main objective to increasing the accuracy and effectiveness of the sensor.

The Yates et al. site-binding model for the electrical double layer, which is discussed further in this chapter, at the oxide/electrolyte interface is widely accepted in this field as the basis for the chemical interactions at the open gate of the sensor [40], [41]. In the site binding model, which is explained in more detail later in this chapter, there are a set number of surface sites available for chemical interactions as the hydrogen ions within the electrolyte react with the oxygen in the oxide. GaO is commonly presently as the material native oxide of the open gate. These reactions have forward and reverse reaction rates, the values of which are not understood as well as the value for the number of surface sites available.

While there are a handful of groups who perform experimental work, only two other groups have completed simulation work with one paper each. This study expands upon simulation work from Bayer et al. [42] and presents a one-dimensional, more extensive model. The time step response, or resolution, of drain current was investigated in the sensor response [1], [9], [29], [35] which is crucial to understanding how the reaction rates play a role in the device sensitivity. Throughout this simulation work, we will only be addressing steady-state response. However, it is clear from the literature that transient response will need to be studied with simulation work in the future once a steady state simulation is successful.

2. Simulation Review

As stated previously, there has been only two other groups to publish work on simulating the AlGaN/GaN HEMT in sensing pH. First, Bayer et al. executed a one-dimensional simulation that linked change in adsorbed charge on the interface to a change in electron density of the conducting channel, resulting in a change in the drain current [42]. In this work transport of the ions in the electrolyte were not included however a simplified model of the charge in the electrolyte was accounted for through Poisson-Boltzmann equation. To execute one-dimensional effects, it was assumed charge distribution was laterally homogenous. While this work was novel, it has limitations in its capability to be expanded past one-dimension to fully represent the pH sensing mechanism of this device. This group also incorporated a reference electrode in their work, noted as U_G. Bayer et al. simulation study tested values of material parameters such as number of available

surface sites, N_S, and dissociation chemical reaction rate constants, K_1 and K_2, to increase sensitivity. They started with N_S as $8x10^{14}$ cm^{-2} to mimic Al_2O_3 as recent experiments indicate the thermal oxide on top of the GaN, Ga_xO_y, behaves similarly to Al_2O_3 [23], [43]. This work also tested N-face polarity of the GaN material and the molar fraction of the AlGaN layer predicting that the N-face polarity of the GaN material will significantly improve the sensing features as well as a reduction in the Al content within the AlGaN layer. Lastly, Bayer et al. ended the study with a brief deduction that the area of the open gate exposed to the electrolyte should be as large as possible relative to the total surface of the device to produce an effective sensor; yet they did not publish evidence to support this reasonable claim. While the simulation study of Bayer et al. excels in its results, the structure modeled did not include the electrical double layer.

The next and more recent simulation study was presented this past year, 2018, by Anvari et al. [44]. Anvari et al. implemented a Triple Layer Model (TLM) developed by Sverjensky et al.[45], [46] which integrates electrostatics of water dipole to the site-binding model [40], [41]. This approach has answered questions of water dipole effect on the reaction where the selectivity of the surface to pH is explained with the TLM equilibrium rates which varied in previous experimental work [23], [47]. Further, Anvari et al. conclude the GaN-based sensor is not as sensitive to ionic type and strength and needs to be coupled with a membrane on its surface to add this functionality [48]. In this work, predictions regarding the relationship between sensitivity and thickness of the surface oxide layer were made where the thin layer of oxide at the surface accounts for the surface chemistry and reaction. The thickness of the AlGaN layer was shown to have a large effect on the 2DEG charge, which is due to the polarization charge, where a decrease in the thickness decreases the charge.

Both Bayer et al. and Anvari et al. lack a comparison to the reports of current-based sensitivity, instead of the potential change with pH. The current-based sensitivity is favorable to report as sensors can more readily report the output current measured. The simulation work of both Bayer et al. and Anvari et al. were completed with finite-difference methods in one-dimension. This approach has made it difficult to expand beyond one dimension to examine geometry dependence of the HEMT sensor. Our past work present two-dimensional finite-element models however both lack the inclusion of the electrical double layer and complex electrochemical kinetics to accurately model the surface reaction[49], [50]. The finite-element simulation method with the electrical double layer we propose in this project can be expanded beyond one-dimension to further the modeling development of the GaN-based HEMT chemical sensor.

To implement the electrical double layer (EDL) in with our past work, a brief review of modeling the EDL with specific adsorption was necessary. Orazem's dissertation work presented an EDL model of a semiconductor-electrolyte interface for a solar cell [51]–[54] which was an extension of Grahame's model [55]. This work was computed with a finite-difference model and focused on the semiconductor modeling for generation and recombination of the solar cell. What is most interesting is how the EDL was modeled as a space charge region, along with the semiconductor. This work also included charge-transfer reactions to allow current to flow from the semiconductor to the solution, which is

not studied in this GaN-based sensor work. However, further simulations with the EDL theory and a semiconductor response are nonexistent. Work found has been focused on metal-electrolyte systems, and effectively modeling electrodes in electrolytes. Guldbrand et al. presented a Monte Carlo study of the force between two charged surfaces [56]. Boda et al. present another Monte Carlo simulation study proving that the Gouy-Chapman theory is not sufficient and the intermolecular potentials, especially for water, need to be added in future models [57]. In another study, for the application of a biosensor measuring protein, Henderson and Boda further support their previous work where it predicts the Gouy-Chapman-Stern (GCS) model isn't enough to accurately model ion selectivity and adsorption of ions [58]. Scaramuzza et al. studied electrode and electrolyte interfaces in COMSOL, MATLAB, and HSPICE, yet all simulation models lacked specific adsorption [59]. Work presented by Wu et al. computed numerical simulations to examine faradic and charging current influence on impedance spectroscopy and the impedance response of a rotating disk electrode, however, these models did not include specific adsorption as well [60], [61].

Simulation Methodology: the Electrical Double Layer

The framework for the TCAD simulation is FLOODS [62] which is suited for III-V devices [63], [64] and is capable of self-consistent, fully-coupled, simulation of reaction-dependent physics occurring at the electrolyte/semiconductor interface. Poisson and continuity of charge carriers are the device equations used to solve charge transport within the electrolyte where ions solely encompass the charge carriers in the electrolyte. The system modeled in FLOODS is shown in Figure 1. The region between the mercury surface and the Inner Helmholtz Plane (IHP) will be defined as the Inner Helmholtz Region. The region between the Inner Helmholtz Plane (IHP) and the Outer Helmholtz Plane (OHP), will be called the Outer Helmholtz Region (OHR). Both the IHR and OHR are simulated as insulators, where there is no charge in the Poisson equation.

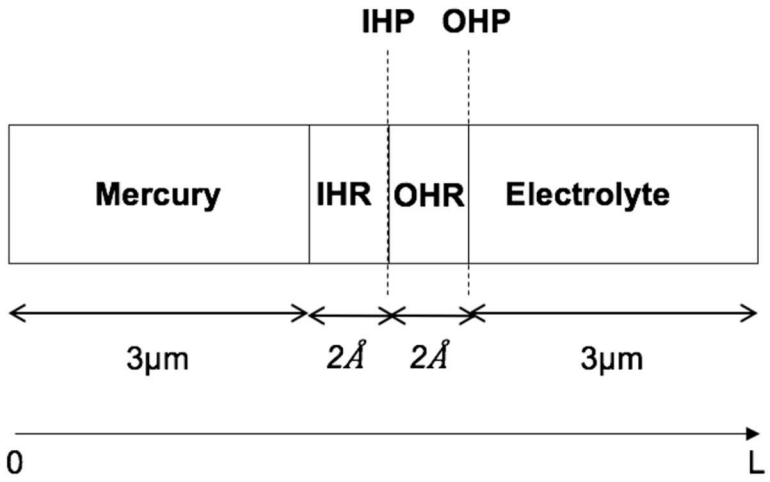

Figure 1. Diagram of the structure simulated in FLOODS to recreate Grahame's mercury drop experiment.

1.1 Electrolyte

The Poisson equation defined within the electrolyte is expressed in equation 3 with permittivity, ε, which is made up by the product of vacuum permittivity, 8.85×10^{-14} F/cm, and the relative permittivity of electrolyte, 78. The elementary charge is expressed as q, 1.6×10^{-19} C, and the ion concentrations sodium and chloride are denoted as $[Na^+]$ and $[Cl^-]$, respectively.

$$\epsilon \nabla^2 \Psi = q([Na^+] - [Cl^-]) \quad (3)$$

Equations 4 and 5 depict ion continuity equations which determine changes in the ion concentration equations relative to time due to drift and diffusion, where the first term is drift and the second term is diffusion.

$$\frac{\partial [Na^+]}{\partial t} = \nabla(q\mu_{Na^+}[Na^+]\nabla\Psi + (D_{Na^+}\nabla[Na^+])) \quad (4)$$

$$\frac{\partial [Cl^-]}{\partial t} = \nabla(q\mu_{Cl^-}[Cl^-]\nabla\Psi + (D_{Cl^-}\nabla[Cl^-])) \quad (5)$$

In these equations μ_{Na+} and μ_{Cl-} are the mobilities and D_{Na+} and D_{Cl-} are the diffusion coefficients of the ions $[Na^+]$ and $[Cl^-]$ respectively. To calculate diffusivity from mobility, Einstein's relation is applied.

1.2 Inner and Outer Helmholtz Regions

Given that charge is assumed not to be retained within the IHR and OHR, the corresponding gradient squared electrostatic potential is equivalent to zero. The Laplace equation for these material layers is expressed in equation 6.

$$\epsilon \nabla^2 \Psi = 0 \quad (6)$$

It is important to note these regions exist only for the purpose of simulating this EDL effect in Finite Element Modeling (FEM). In EDL theory, these regions do not exist since ions can only exist at the planes (IHP and OHP) and the space in between the planes is atomic spacing as an ion cannot physically fit in between the two planes of charge. Refer to Figure 2 for a visual aid. To simulate this in FLOODS, a FEM tool, these regions had to be created, however we made the grid spacing small enough so an ion could exist only at the boundaries, and effectively ions simulated in these regions could exist only at the IHP and OHP.

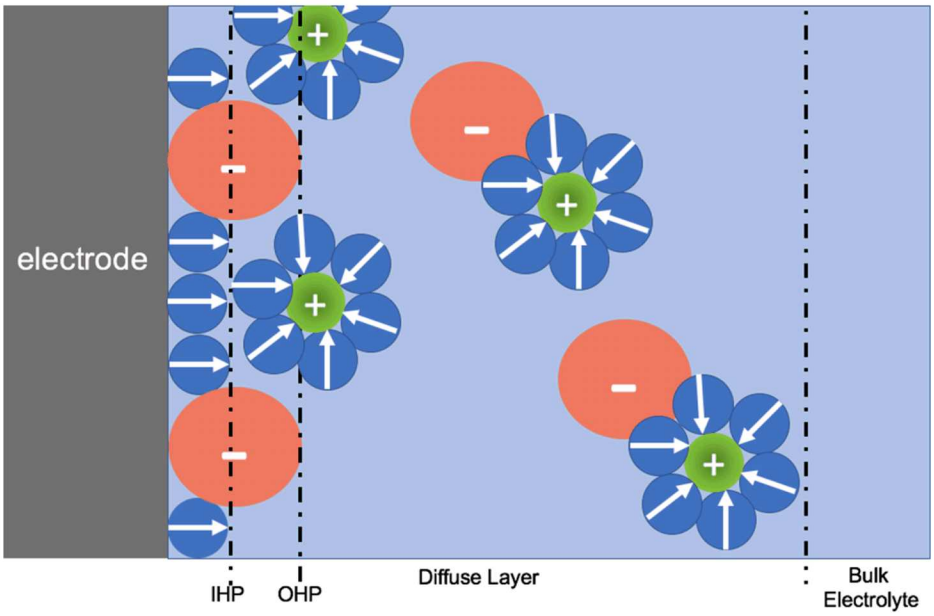

Figure 2. Three planes of charge comprise the Stern model: Inner Helmholtz Plane (IHP), Outer Helmholtz Plane (OHP), and Diffuse Layer. The IHP is the plane of closest approach for small ions nearest to the electrode. The OHP is the second plane away from the electrode where larger ions and solvated ions are shown. The IHP and OHP form the compact layer and behaves as the Helmholtz Model. The Diffuse Layer is in between the compact model and the bulk electrolyte where the ions diffuse according to the Gouy-Chapman model.

1.3 Specific Adsorption

In the Gouy-Chapman-Stern (GCS) theory, there is no specific adsorption, but nonspecific adsorption. The chemical reaction described in this section is not included in FLOODS simulations for the GCS model. This reaction is included only when specific adsorption is explicitly stated. To replicate Grahame's experimental results, specific adsorption at the IHP must be implemented. In this case, chloride ions (Cl^-) are adsorbed on the mercury surface. Both the IHR and OHR are still treated as insulators but now there is transport of chloride ions from the electrolyte through the OHR to adsorb on the IHP. Since the OHR is treated as an insulator, it has no ion concentration defined within it. Therefore, we must allow chloride ions to transport from the electrolyte into the OHR to be adsorbed on the IHP. Grahame does not explicitly list the chemical reaction taking place in his work [55] therefore we implemented only one simple chemical reaction where one chloride ion bonds with mercury to form a neutral compound. Below is the reaction, followed by the differential equation for the reaction where the reaction rates are simplified to a forward reaction rate, K_f, and a reverse reaction rate, K_r.

$$[\mathrm{Cl-Hg}] \leftrightharpoons [\mathrm{Cl^-}] + [\mathrm{Hg^+}] \tag{7}$$

$$\mathrm{K_f}[\mathrm{Cl^-}][\mathrm{Hg^+}] - \mathrm{K_r}[\mathrm{Cl-Hg}] + \frac{\partial}{\partial \mathrm{t}}[\mathrm{Cl-Hg}] = 0 \tag{8}$$

The number of available surface sites, denoted here as N_S, is questioned among researchers in this field since it is an important variable in the chemical reaction kinetics. However, if we examine Grahame's work, in particular Grahame's figure 9 [65], where he calculates components of charge within the EDL, we can use the value of adsorbed charge to determine an appropriate value for N_S in FLOODS to replicate his work and for

a safe assumption in this variable moving forward. If we look at a maximum value of adsorbed charge, at -0.1 E^{-}, it is roughly 28 $\mu C/cm^2$. This value, multiplied by the elementary charge, is approximately $1.8x10^{14}$ cm^{-2}. From this, a safe assumption of N_S is $2x10^{14}$ cm^{-2} was used in these simulations.

There have been lingering questions of what detail is required in modeling the reaction rates; constants versus exponential dependence on potential [44]. It is well accepted that reactions are dependent on potential and this is expressed as the reaction rates being exponentially dependent on potential [66], [67]. The work presented in this chapter studied the effects of the equilibrium rate having an exponential dependence on potential in steady-state. The exponential dependence was implemented on the forward reaction rate and is expressed in equation 9. It is critical to note that the potential dependence on IHP is with respect to the potential at the bulk of the electrolyte. In our FLOODS simulations the potential in the bulk electrolyte was set to zero. Faraday's constant is represented as F. Temperature is written as T and R is Boltzmann's constant. The symmetry factor, β, was assumed to be 0.5 and this approximation is well accepted for this work [51], [67].

$$K_f = K_{fo} * \exp[\frac{(1-\beta)F}{RT}](\Psi_{\text{Bulk Electrolyte}} - \Psi_{IHP}) \quad 9$$

The reaction rate was tuned until the charge and voltage behaviors matched Grahame's results because we had no a priori estimates [55], [65]. In the optimization testing, the reverse reaction rate was set to a constant value, 10^{-11}, and the forward reaction rate was incremented for each simulation loop. Each loop would apply the electrode bias, ranging from 0V to ~0.5V, and would output the value of adsorbed charge. To obtain a potential and charge distribution profile from Grahame's work [55], the goal of the optimization curve was to have $10^{11}cm^{-2}$ adsorbed charge at the starting bias point, 0V, and where the last bias point, 0.474V, would result in adsorbed charge nearly the value of the total surface sites available, N_s, which was $2x10^{14}$ cm^{-2} in this case. This optimization test resulted in two different forward reaction rate constant values; here these values will be denoted as a low equilibrium rate (for the low value of adsorbed charge) and a high equilibrium rate (for a high value of adsorbed charge). These values were optimized in the mercury drop environment with the electrolyte of 0.3M NaCl as this is the molarity Grahame used for his work presented in his Figure 4 and Figure 9 [55].

1.4 Boundary Conditions

The electrostatic potential and solution variables are defined to specific values, using Dirichlet boundary conditions, at two points of the structure simulated here: the electrode (mercury) contact and the bulk of the electrolyte. The electrode contact has an applied bias which is used to replicate Grahame's work. The electrolyte potential is fixed at the bulk to zero to replicate Grahame's work [55].

$$\psi|_{x=0} = V_{\text{applied bias}} \quad 10$$

$$\psi|_{x=L} = 0 \quad 11$$

The solution variables for ion concentrations are fixed to their bulk value at the boundary of the electrolyte due to the thickness of the electrolyte is more than ten Debye lengths. The bulk value of the concentrations is dependent on the molarity of the concentration used for the simulation. For 0.3M, the bulk concentration for both Na and Cl is $1.8x10^{20}cm^{-2}$. At 1M, the bulk concentration for both Na and Cl is $6.02x10^{20}$ cm^{-2}.

$$[Na^+]|_{x=L} = [Na^+_{bulk}] \quad 12$$
$$[Cl^-]|_{x=L} = [Cl^-_{bulk}] \quad 13$$

2 Calculating Integral Capacitance in FLOODS

The results of FLOODS simulations will be examined as capacitance curves to easily compare to Grahame's work. For large signal capacitance of the electrolyte, the total excess charge in the electrolyte (Na-Cl), σ, is integrated over the area of the electrolyte. This is multiplied by the elementary charge, q, and then divided by the voltage difference between the OHP, ϕ_{OHP}, and the bulk of the electrolyte (which is set to zero).

$$C_{Diffuse} = \frac{\sigma_{Diffuse} * q}{\Phi_{OHP} - 0} \quad 14$$

Since the Inner Helmholtz and the Outer Helmholtz regions (IHR and OHR) are treated as insulators, the capacitance in both of these regions are computed as parallel-plate capacitors, which is true to the Helmholtz theory. The thickness of each region was set to 2 Å to mimic Grahame's structure [55]. The dielectric constant was set to 7 producing a capacitance value of 31 $\mu F/cm^2$.

$$C_{IHP} = C_{OHR} = \frac{\epsilon_0 \epsilon}{d} = 31 \frac{\mu F}{cm^2} \quad 15$$

To compute the total capacitance of the EDL model, the capacitances of the three regions are in series and the classic formula of capacitors in series will be applied to this simulated structure. The total capacitance is expressed in equation 16 where the region with the smallest capacitance dominates the total capacitance.

$$\frac{1}{C_{total}} = \frac{1}{C_{IHR}} + \frac{1}{C_{OHR}} + \frac{1}{C_{Diffuse}} \quad 16$$

Results: Simulating EDL

First the simple EDL theory of GCS model was simulated in FLOODS where no chemical reaction was implemented. The total large signal, or integral, capacitance of this structure is shown in 3 at varied electrolyte concentrations. Matching the theoretical GCS model, results from FLOODS capture the minimum, or "dip", in the capacitance curves as increasing magnitude with increasing electrolyte concentrations [66], [68]. To start simply with the specific adsorption model, the equilibrium rates were set as constants. The FLOODS script was optimized to retrieve a forward reaction rate to achieve an increase in adsorbed sites with increase in bias, to replicate Grahame's work [55]. In this optimization, the reverse reaction rate remained at a constant value. The most optimum case observed was an adsorbed concentration increase by 4 times over a potential change from 0 to ~0.5V (the bias range used in Grahame's work [55]). However this

increase in adsorbed charge was not sufficient to achieve the potential drop Grahame displayed, shown in Grahame's Figure 4 [55].

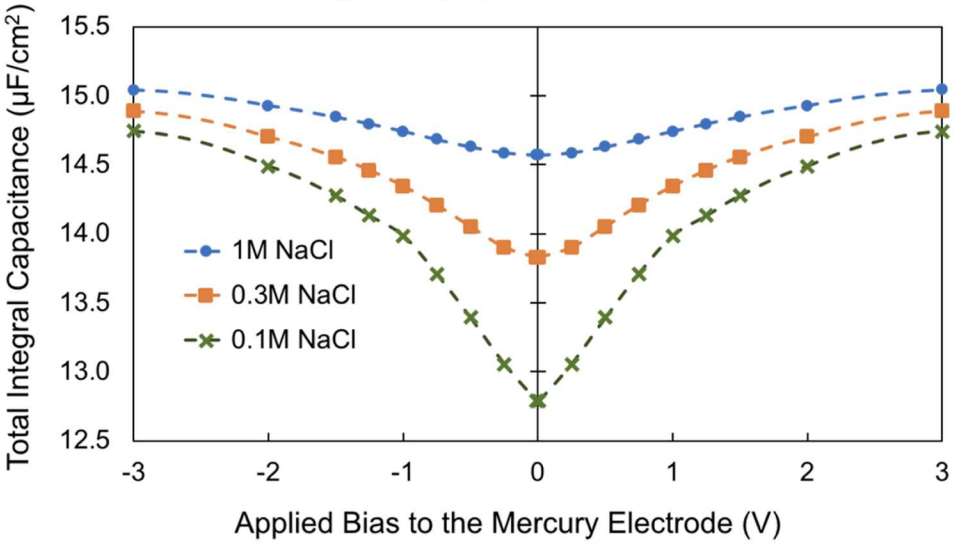

Figure 3. Total integral (or large signal) capacitance in microfarads per square centimeter as a function of applied bias to the mercury electrode produced from FLOODS simulation of Gouy-Chapman-Stern model.

Both low and high equilibrium constants were analyzed with the large signal, or integral, and small signal, or differential, approach in FLOODS to obtain integral and differential total capacitance curves to compare further to Grahame's work [55], [66]. This model was also tested in various concentrations of the NaCl electrolyte to observe the capacitance dependence on the electrolyte, since GCS does not have a reaction take place. These results are shown in Figures 4 and 5.

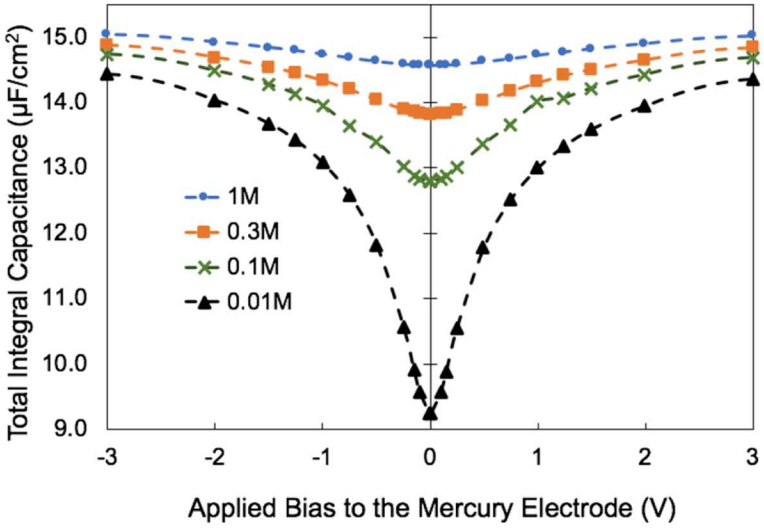

Figure 4. Large signal, or integral, capacitance with respect to applied bias for a low equilibrium rate.

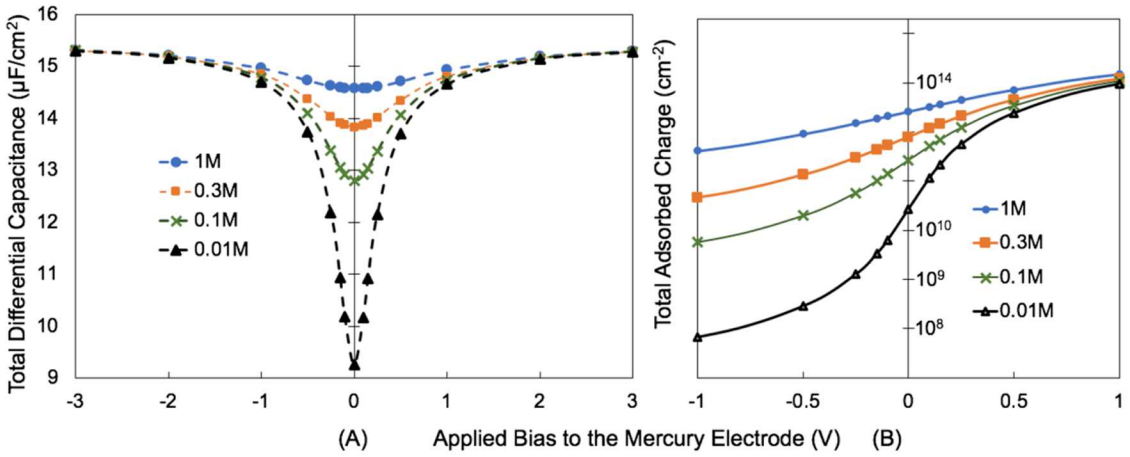

Figure 5. Small signal, or differential, capacitance (A) and the adsorbed charge (B) with respect to applied bias for low forward reaction rate.

Between the two cases of the low and high equilibrium rates is a shift in the minimum, or "dip", of both the integral and differential capacitances. This minimum is defined as the electrocapillary maximum [55], [66] and is a point of zero charge. In the case with the low equilibrium rate, the minimum is at 0V, but this shifts towards a positive voltage when the high forward reaction rate is applied. This result is agreeable with the notion that there is more adsorbed charge on the surface and therefore the adsorbed charge causes a shift in the potential needed to achieve an electrocapillary maximum, where the total charge is equal to zero. What is also interesting to observe is that the slope of the minimum decreases as the concentration of NaCl increases. It is interesting this behavior is observed in this model with specific adsorption where the behavior is also observed in the GCS model; suggesting it is independent of adsorption.

However these simulation results lack the accurate potential versus depth profile (to match Grahame's work in his Figure 16 [55]). The negative applied bias region is due to its absence of specific adsorption. The positive applied bias observes a "cross-over"; as applied positive bias increases, the potential at the IHP decreases (increasing in magnitude however becoming more negative). This is due to a large amount of adsorbed charge from the specific adsorption reaction. At a constant reaction rate, this potential "cross-over" is not observed which has prompted further exploration into reaction rates with exponential dependences on potential.

Next, the reaction rates with exponential potential dependence were implemented. These results are shown in 6 and 7. Near the electrocapillary maximum is a little hump. Grahame observed these "humps" in his experiments (Grahame's Figure 4 [55]) and attributed this behavior to electrostatic repulsion from ions within the double layer. This phenomenon is implemented in FLOODS only in the diffuse part of the double layer; not within the IHR and OHR. This explanation could partially account for the "humps" observed in FLOODS results and therefore this methodology is more "realistic" however, Grahame does not account for this electrostatic repulsion of ions in the EDL in his computations.

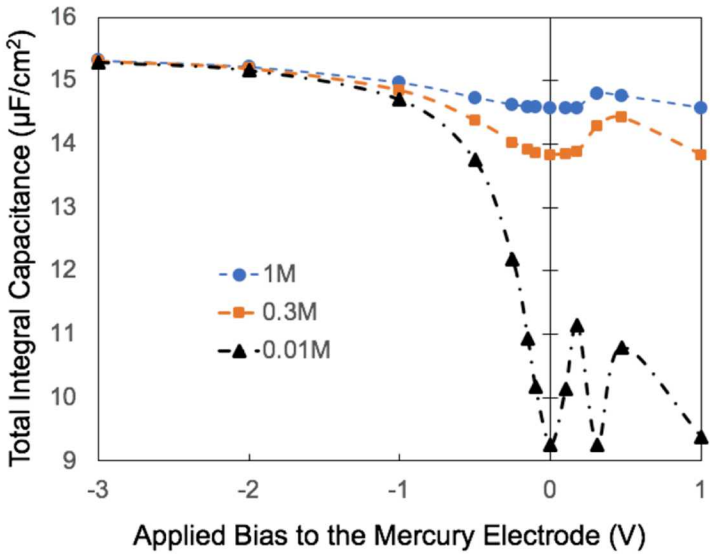

Figure 6. Large signal, or integral, capacitance with respect to applied bias for an equilibrium rate with exponential dependence on potential.

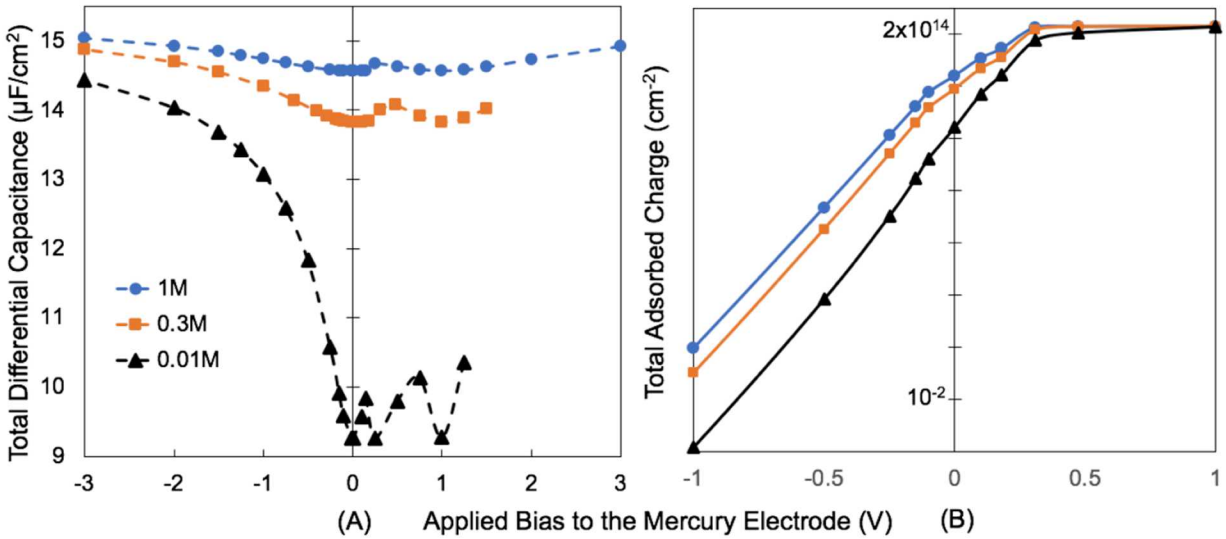

Figure 7. Small signal, or differential, capacitance (A) and the adsorbed charge (B) with respect to applied bias for an equilibrium rate with exponential dependence on potential.

The components of charge were also examined in this model and are presented in Figure 8. Everything matches Grahame's work, in Grahame's Figure 16 [55], except for the charge of the chloride in the diffuse region of the EDL. In FLOODS a pile up of chloride is observed at high applied bias which is to be expected as it is negatively charged and would be attracted to the mercury surface for high positive potentials. In FLOODS, there are two regions of excess charges, 0.10V to 0.18V and again from 1.25 to 1.5V. This is credible given that at high bias the adsorbed charge is nearly maxed out at the number of surface sites available, N_s, so the chloride is no longer used in the reaction and accumulates. For the other range of smaller positive bias points, the chloride ions accumulation could be a result of a limiting forward reaction rate; where the reaction rate isn't large enough to allow for 100% adsorption at the surface, (where the rate isn't fast

enough to allow the reaction to fully adsorb) so the chloride has excess ions as a result. However this profile of excess chloride in the diffuse part of the EDL differs from Grahame's work [55] where excess chloride charge is constant at approximately 4 $\mu C/cm^2$, even at a negative applied bias. This is speculated to be a result of existing positive surface charge on the mercury electrode which attracts the chlorine to the surface. Since each bias point of Grahame's work is a new mercury droplet, a new surface is created at each bias point and with existing positive surface charge on the mercury electrode.

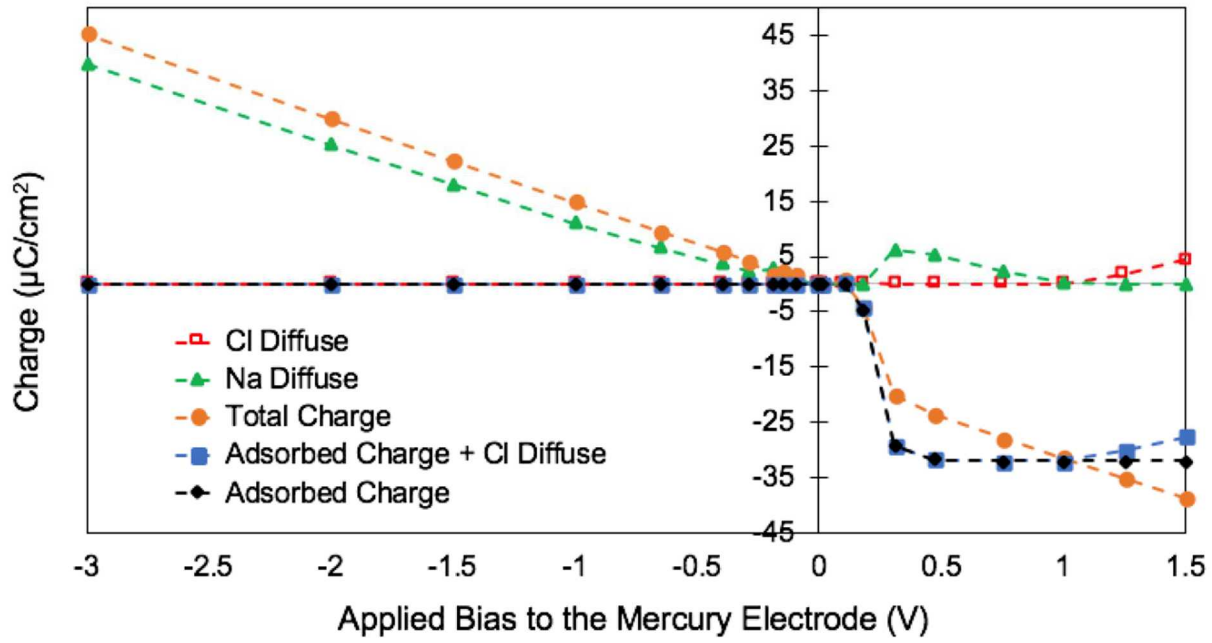

Figure 8. Components of charge in the EDL, between the mercury electrode and the start of the bulk of the electrolyte at room temperature for 0.3M NaCl.

It is worth noting that the potential versus depth profile of this model was successfully tuned to match Grahame's [55]. The potential profile achieved from these simulations in FLOODS is shown in Figure 9. This cross-over behavior, where larger positive applied biases had a more negative potential at the IHP, could only be achieved with equilibrium rate exponential dependence on potential.

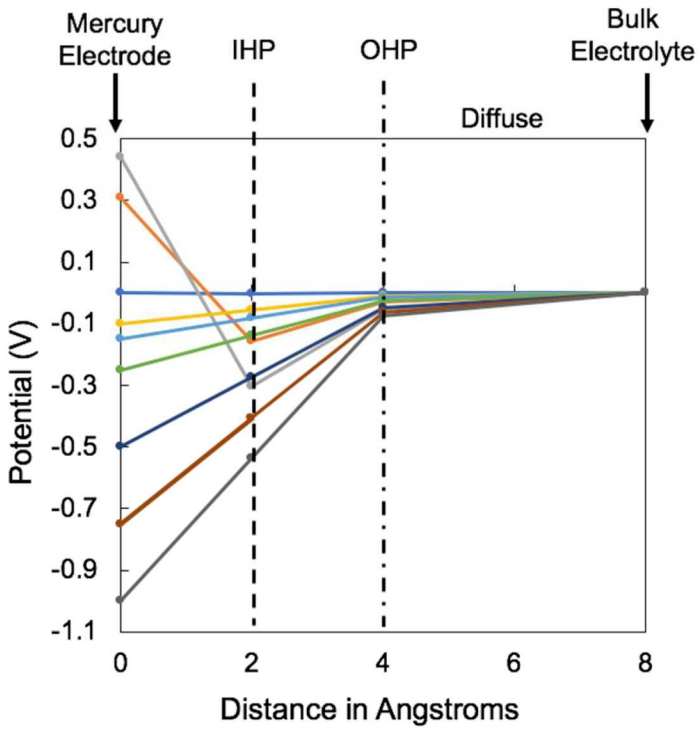

Figure 9. Potential in the EDL between the mercury electrode (left) and the end of the diffuse region of the EDL (right) for a 0.3M NaCl solution at room temperature at various applied electrode biases. These values were calculated in FLOODS for the equilibrium rate as an exponential dependence on potential.

These different scenarios of implementing the EDL should be compared to understand what is needed to effectively model the EDL in FLOODS for this mercury drop experiment. The difference between the integral and differential capacitance is minimal and therefore using only one of the two for further studies is sufficient. Examining these integral and differential capacitance graphs between the high and low equilibrium constants, as well as the equilibrium rate with an exponential dependence on potential (to simulate Grahame model), shows the same behavior as well as the same maximum and minimum capacitance values. The difference between the reaction rates as a constant and the equilibrium rates as an exponential dependence does show a difference in behavior near the electrocapillary maximum, however the value of the capacitance does not show major differences.

4.3.1 Comparison of Models

For the equilibrium rate, the significance of an exponential dependence on potential is depicted in Figure 10 and 11. While Figure 4-10 is the integral capacitance and Figure 4-11 is the differential capacitance, the same trend is observed. The exponential dependence on potential combines the low constant reaction rate function with the high constant reaction rate function and therefore producing a “hump”. The behavior of the exponential dependence on potential in the forward reaction rate with electrostatic repulsion from ions in the diffuse region of the double layer defines the “humps” Grahame observed in his experimental work shown in Grahame’s figure 2 [65].

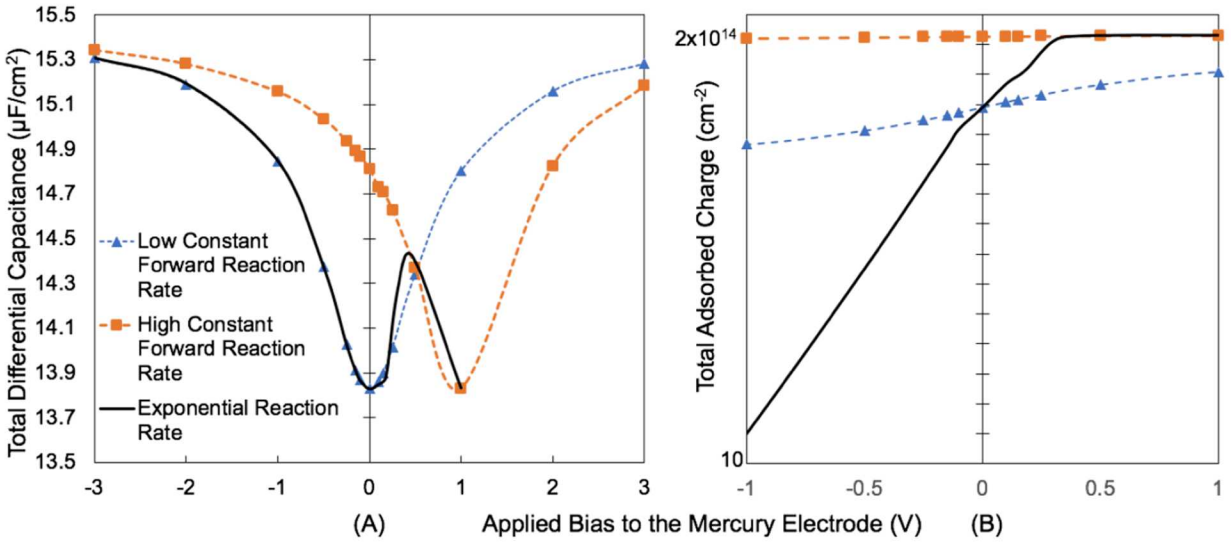

Figure 10. Integral Capacitance Comparison of Models. (A) Integral capacitance of three different models. (B) Adsorbed charge for each model.

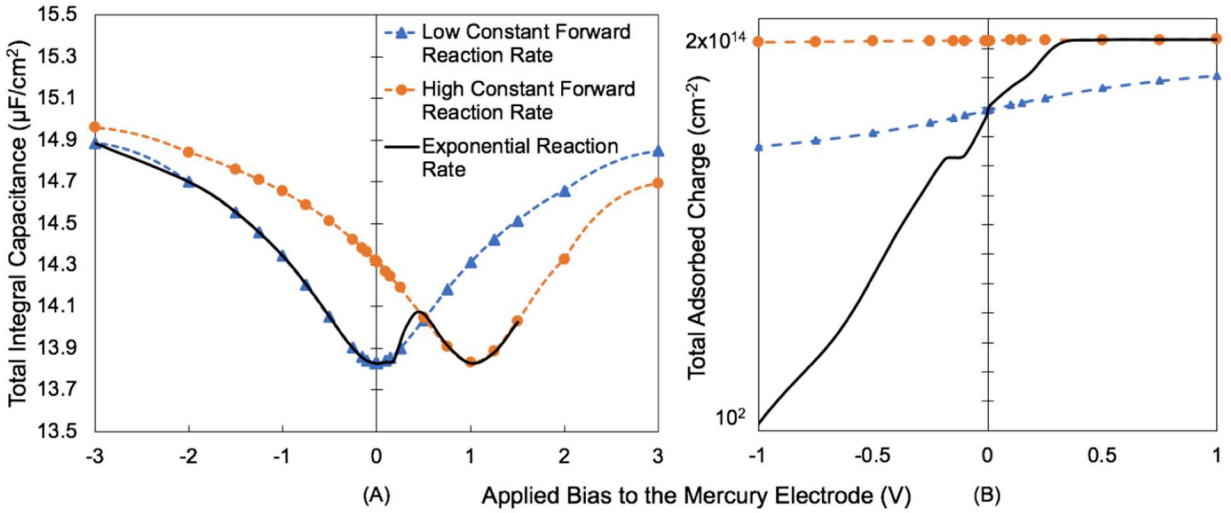

Figure 11. Differential Capacitance Comparison of Models. (A) Differential capacitance of three different models. (B) Adsorbed charge for each model.

4.3.2 Importance of the IHP and OHP

A concern in modeling is understanding the simplest model needed to produce accurate results in order to save computation time. A quick simulation study was conducted to understand the importance of the IHP and OHP regions. The forward reaction rate with exponential dependence on potential was used in Figure 1 however the reaction was modified to take place at the OHP; extending the IHP to the OHP and not modeling an extra region such as OHR. This study produced the exact same capacitance results revealing that, from a computation perspective of this simple case, the Outer Helmholtz Region is not significant. However, if more work is to be done on investigation of the electrolyte complexities, such as of size variation of molecules and competing reactions, the OHP could add more significance to simulation results. However, the addition of the

OHP is believed to increase convergence at larger applied biases to avoid for an unphysical buildup of charge at the interface. It also does not add a significant computation time, therefore it should be added and kept in models for increased accuracy.

Simulation Methodology: Open-Gated High Electron Mobility Transistor as pH sensor

Poisson and continuity of charge carriers are the device equations used to solve charge transport within the semiconductor and electrolyte. Electrons and holes comprise the charge carriers within the semiconductor materials whereas ions solely encompass the charge carriers in the electrolyte. The device simulator solves for solution variables originating from two partial differential equations: Poisson's equation for electrostatics (17) and charge continuity (18). The electrostatic potential, Ψ, is continuous throughout the device structure. The total charge in a material is σ_{total}, c_i refers to the concentration of a charged species i, and N_i is the flux density of the species modeled with drift and diffusion related expression corresponding to each material.

$$\nabla^2\Psi = -\frac{\sigma_{\text{total}}}{\epsilon} \quad 17$$

$$\frac{\partial c_i}{\partial t} = -\nabla N_i \quad 18$$

1. Device Structure

Figure 12a illustrates a two-dimensional rendering of the structure tested through the simulation framework. Figure 12b displays a cross-sectional view with labeled polarization charges. The device structure is comprised of a 3 μm electrolyte, 2Å Outer Helmholtz Region (OHR), 2Å Inner Helmholtz Region (IHR), a 15 nm AlGaN layer, 1.8 μm GaN buffer layer, and a 1.3 μm substrate layer of AlN and SiC. All the layers are realistic dimensions with the exception of the electrolyte layer being scaled large enough for simulating transport characteristics.

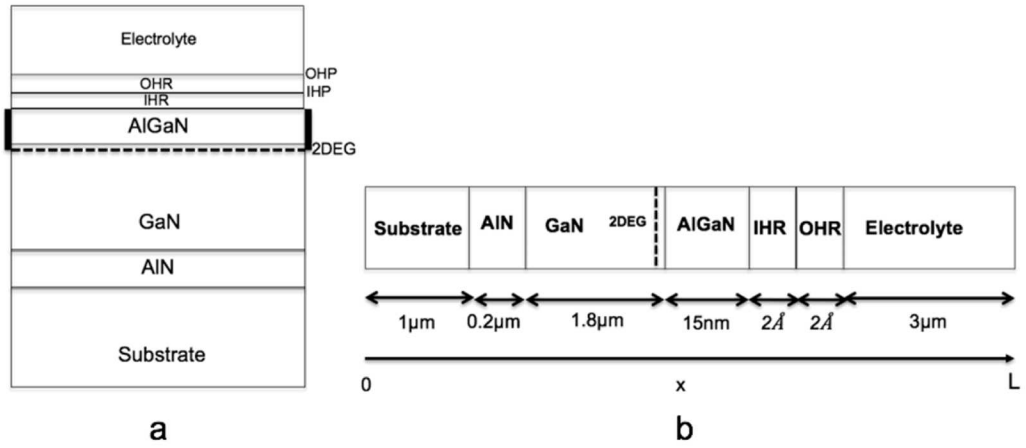

Figure 12. 2-D rendering of GaN-based HEMT structure simulated in FLOODS. (a) Two-dimensional design of the GaN-based HEMT structure. The un-metalized gate area includes the electrolyte and double layer regions. (b) Vertical cross-section displaying the thickness of each layer for the GaN-based HEMT.

2.2 Two-Dimensional Electron Gas

Ga-face polarization model was used in which the AlGaN undergoes tensile strain to result in an induced piezoelectric positive polarization charge, σ_{pol2}, at the AlGaN-GaN interface [69], [70]. The bottom of the GaN buffer layer has a positive charge, σ_{pol1}, with a value of 2.2×10^{13} cm^{-2}. The spontaneous polarization charge cancels at the AlGaN-GaN interface and the remaining the piezoelectric polarization of the AlGaN produces a net positive charge, σ_{pol2}, of 1.06×10^{13} cm^{-2}. The net negative polarization charge, which is the sum of the spontaneous and piezoelectric polarization charges, is implemented as σ_{pol3}, valued at 3.26×10^{13} cm^{-2}, located at the top of the AlGaN. These polarization charge values used in the device structure for simulation testing were acquired from the Ambacher group [69].

2.3 Electrolyte

The Poisson equation within the electrolyte is defined in equation 19 with permittivity, e, (vacuum permittivity, 8.85x10-14 F/cm times relative permittivity of electrolyte, 78), the elementary charge q, 1.6x10-19 C, and the ion concentrations sodium $[Na^+]$, chloride $[Cl^-]$, hydrogen $[H^+]$, and arbitrary anion to react with hydrogen $[A^-]$.

$$\epsilon \nabla^2 \Psi = q([Na^+] - [Cl^-] + [H^+] - [A^-]) \quad (19)$$

Ion continuity equations for the electrolyte are depicted in equations 20 through 23 which determine changes in the ion concentration relative to time due to drift and diffusion where the first term is drift and the second term is diffusion. Therefore μ_{Na+} , μ_{Cl-} , μ_{H+}, and μ_{A-} are the mobilities and D_{Na+} , D_{Cl-} , D_{H+} , and D_{A-} are the diffusion coefficients of the ions $[Na^+]$, $[Cl^-]$, $[H^+]$, and $[A^-]$ respectively. To calculate diffusivity from mobility, Einstein's relation is applied.

$$\frac{\partial [Na^+]}{\partial t} = \nabla(q\mu_{Na^+}[Na^+]\nabla\Psi + (D_{Na^+}\nabla[Na^+])) \quad (20)$$

$$\frac{\partial [Cl^-]}{\partial t} = \nabla(q\mu_{Cl^-}[Cl^-]\nabla\Psi + (D_{Cl^-}\nabla[Cl^-])) \quad (21)$$

$$\frac{\partial [H^+]}{\partial t} = \nabla(q\mu_{H^+}[H^+]\nabla\Psi + (D_{H^+}\nabla[H^+])) \quad (22)$$

$$\frac{\partial [A^-]}{\partial t} = \nabla(q\mu_{A^-}[A^-]\nabla\Psi + (D_{A^-}\nabla[A^-])) \quad (23)$$

The electrolyte is NaCl with a concentration of 100 mM. HA characterizes an acid in the electrolyte where H^+ is a hydrogen cation and A^- is a corresponding anion. In this simulation testing, the hydrogen concentration ranges from 10^{-2} mM to 10^{-9} mM. The pH is determined through the negative log of the hydrogen concentration. This simulation ensured electroneutrality in the electrolyte by setting a condition where the concentration of A^- always equals H^+. The flux of species due to convection is assumed to be negligible and is not modeled in this simulation.

2.4 Semiconductor

The Poisson equation in the AlGaN, GaN, and substrate semiconductor layers of the device are expressed in equation 24. The variables n and p are the electron and hole carrier concentrations, and N_D and N_A are the donor and acceptor impurity concentrations. The GaN layer was assigned a donor doping of 10^{16} cm^{-2} to model n-type

doping whereas smaller donor concentration values of 10^{12} cm^{-2} were assigned to model unintentionally doped regions. No acceptor doping was simulated in this study.

$$\epsilon\nabla^2\Psi = q(n - p + N_D - N_A) \quad 24$$

The continuity equations for electrons and holes in the semiconductor material are dependent on Quasi-Fermi energy levels, ϕ_{fn} and ϕ_{fp} , as presented in equations 25 and 26. This computation captures drift-diffusion physics and is most compatible for simulating heterostructure based devices. The Quasi-Fermi energy levels are continuous throughout the semiconductor and are analogous to electrochemical potentials. The Maxwell-Boltzmann distributions for electron and hole concentrations with respect to the Quasi-Fermi levels and the conduction, E_c, and valence, E_v, energy bands are expressed in equations 27 and 28. N_c and N_v are the density of states for electron and holes respectively, and V_t is the thermal voltage at room temperature (0.0259 eV).

$$\frac{\partial n}{\partial t} = -nq\mu_n\nabla^2\phi_{f_n} \quad 25$$

$$\frac{\partial p}{\partial t} = -pq\mu_p\nabla^2\phi_{f_p} \quad 26$$

$$n = N_c e^{\frac{-(E_c-\phi_{f_n})}{V_t}} \quad 27$$

$$p = N_v e^{\frac{-(E_v-\phi_{f_p})}{V_t}} \quad 28$$

In this simulation, the electrostatic potential, Y, defines the vacuum energy level, which is related to conduction band through electron affinity; $E_c = \Psi - \chi$. This method can be correlated to multiple semiconductor materials with different energy band gaps to be given a similar reference energy level. A low-field mobility model was used after the Farahmand group [71]. Since this device is based on a wide-bandgap material, neither recombination nor generation of charge carriers occurs in the simulation.

2.5 Oxide

Given that charge is assumed not to be retained within the oxide, the corresponding electrostatic potential is equivalent to zero. The Poisson equation for these material layers is depicted in 29.

$$\epsilon\nabla^2\Psi = 0 \quad 29$$

2.6 Interface Regions

The polarization charges previously discussed are added to the Poisson equation at their designated semiconductor interfaces. The interface of most interest is the interface of the electrolyte/AlGaN which translates to the sensor mechanism of the device. The GaN-based HEMT pH sensing capability originates from the hydrogen ions available at the un-metalized gate surface altering conductive channel current. The site-binding model for oxides [40], [41] was used to simulate the amphoteric nature of the electrolyte and semiconductor interface and is shown in equations 30 and 31. S denotes an oxide molecular site with OH, a bonded hydroxyl group, resulting in creating a positively charged, SOH^+_2, and negatively charged, SO^-, sites, respectively, from neutral sites, SOH.

$$[S-OH_2^+] \rightleftharpoons [S-OH] + [H^+] \quad 30$$

$$[S-OH] \rightleftharpoons [S-O^-] + [H^+] \quad 31$$

These chemical reactions are executed in FLOODS via rate equations 32, 33, and 34. The differential equations for reactions 30 and 31 to be computed with adsorption, K_1 and K_3, and dissociation, K_2 and K_4, rate constants are expressed in equations 32 and 33. The reaction rate constants were tuned as fitting parameters to match the existing literature and achieve a maximum concentration of positive surface sites at low pH and a maximum concentration of negative surface sites at high pH. The boundary condition for the number of available surface sites is expressed in equation 34. N_S is the number of available sites at the surface, which was set to a maximum of $1x10^{15}$ cm^{-2}. Bayer et al. validate this assumption with work from Bergveld et al. [42], [43]. Therefore, all the possible sites, being positive, negative, or neutrally charged, must be equal to the number of available bonding sites, N_S.

$$K_1[S-O^-][H^+] - K_2[S-OH] + \frac{\partial}{\partial t}[S-O^-] = 0 \quad 32$$

$$K_3[S-OH][H^+] - K_4[S-OH_2^+] + \frac{\partial}{\partial t}[S-OH_2^+] = 0 \quad 33$$

$$[S-OH] = N_S - [S-O^-] - [S-OH_2^+] \quad 34$$

The sensitivity (mA/mm-pH) of the device is defined as the slope of the current versus pH plot (I/pH). The simulated drain current decreasing with increasing pH, which is a result supported by other experimental studies [1], [9], [23], [30], [32]–[35], [37]–[39]; this results in negative sensitivity values. The objective of this work is to increase the magnitude of the sensitivity, where consequently sensitivities are typically presented as the absolute value. Throughout this work, sensitivities will be presented as absolute values.

2.7 Boundary Conditions

The electrostatic potential and Quasi-Fermi levels solution variables are defined to specific values, using Dirichlet boundary conditions, at two points of the device: the bottom of the substrate and the top of the electrolyte. The substrate is given a reference potential of zero. However, the electrolyte contact is fixed at 3.7eV to match the HEMT fermi level. Yet when the pH of the electrolyte changes, the Nernst value of 59mV is added or subtracted to the electrolyte. The electrolyte potential is pinned to the pH potential value with respect to the HEMT equilibrium fermi energy level. The solution variables for ion concentrations are fixed to their bulk value at the boundary of the electrolyte due to the thickness of the electrolyte is more than ten Debye lengths.

Results: pH GaN-based HEMT sensor with EDL and specific adsorption finite-element modeling

The HEMT sensor was simulated in FLOODS and modeled via a 1-D structure to study the effect of equilibrium rates, AlGaN surface charge ($\sigma_{AlGaN/IHR}$), and number of available surface sites (for adsorption in the reaction, N_S). Also included in this chapter are

preliminary results of a drain bias dependence. A comparison of simulated and experimental current-based sensitivity is discussed in the following chapter.

The three major parameters were tested in this 1-D simulation (equilibrium rates, AlGaN surface charge, and number of available surface sites) to achieve a sensor response. Only variations in the number of available surface sites resulted in a sensor response. Once a sensor response was achieved, the effects of the remaining two parameters were tested to understand their relationship with the sensor response. The key figure of merit discussed in this work to quantify the sensor response is the concentration of charge in the channel, or 2DEG charge in HEMT devices, since it is directly proportional to current. Current in a channel for a linear region of operation can be expressed as:

$$\mathrm{I} = \frac{\mathrm{Q}\mu\mathrm{V_{DS}W}}{\mathrm{L}} \tag{35}$$

The 2DEG channel charge concentration is noted as Q, the mobility is noted as μ, L is the channel gate length, W is the channel gate width, and V_{DS} is the applied drain bias. For the remainder of this chapter, only the concentration of 2DEG channel charge, Q, is examined as all other values are assumed constant for this 1-D simulation. The number of surface sites available, N_S, is largely dependent on the material at the top of the semiconductor, which is the interface with the electrolyte. This top layer is typically a native oxide. N_S is the physical displacement of how many adsorption sites can take place per area on the oxide surface. Since a bond length is fixed, there is a physical limitation to the number of surface sites available. Since FLOODS could not simulate above a N_S value of $9x10^{14}$ cm^{-2} due to convergence issues, below is an investigation of this physical limitation of 10^{15} cm^{-2}.

$$\mathrm{N_S} = \frac{10^{15}}{\mathrm{cm^2}} * \frac{1\mathrm{cm^2}}{10^{16}\mathrm{\AA^2}} = \frac{1}{10\mathrm{\AA^2}} \tag{36}$$

10^{15} surface sites in an area of 1 cm^2 is equal to 1 surface site for an area of 10 $Å^2$. The lattice constant for GaN is 3.186 Å and 5.186 Å depending on the growth and plane of the AlGaN/GaN stack [72], and the area could be 10.15 $Å^2$ or 26.89 $Å^2$. If we consider the hydrogen bond length of a water molecule is 2Å, this physical limitation for the number of surface sites is reasonable. Therefore, the value calculated in equation 36 is a maximum value of number of available sites; predicting the most available surface sites physically possible for this oxide.

3.1 Understanding the 2DEG as a Sensor Response

Since a maximum number of available adsorbed sites was previously determined and a minimum value was needed to achieve a sensor response, further investigation into this range of available surface sites was explored to determine a relationship between the number of surface sites and the sensor response. In a small range where N_S is varied between 10^{11} and 10^{13} cm^{-2}, the response of the channel charge, diffusion charge, and interface charge were studied. An expected result was observed, where the interface charge increased to compensate for the new increasing N_S value. A slight change in the

channel charge behavior is observed yet the total change in channel charge concentration with pH, or sensitivity, does not increase in magnitude to increase the sensor response. This phenomenon is due to the diffusion charge still compensating for the interface charge. Higher values of N_S were evaluated to determine the effect on channel charge, diffusion charge, and interface charge. These results are shown in Figure13. With the largest value of N_S there is a significant shift from negative to positive in the total diffuse charge resulting in increased change in the channel charge with pH, or in other words, an increased sensitivity. Further investigation into the potential profiles are reviewed to explain this result.

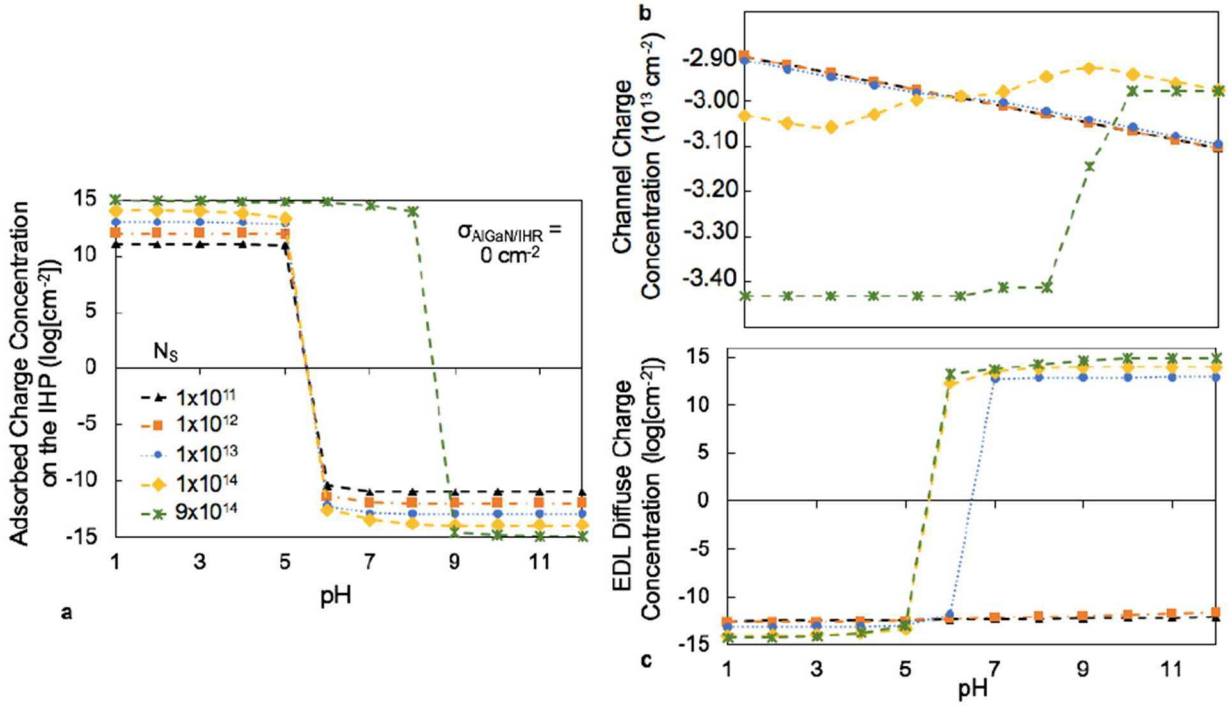

Figure 13. HEMT sensor response to extreme values for the number of available surface sites, N_S. (a) The adsorbed charge concentration at the IHP. (b) The electron concentration, 2DEG channel charge, concentration in the conducting channel. (c) The total charge concentration in the diffuse part of the EDL.

The potential as a function of depth, or potential profile, for a low value of N_S, 10^{11} cm^{-2}, is displayed in Figure 14 where the full device depth is in part a and part b is zoomed in for a potential profile of the EDL structure (at the electrolyte/semiconductor interface). In part a, -3μm is the bulk of the electrolyte solution and +3μm is the backside of the SiC. The potential of the bulk electrolyte is controlled by the pH where an ideal Nernst behavior (59mV decrease in potential with increasing pH) was controlled in the simulation boundary conditions. In this case, where N_S is low, there is small change in potential at the electrolyte/semiconductor surface. The same potential profile was also studied for the case where N_S is large, $9x10^{14}$ cm^{-2}, and is shown in Figure 15. The zoomed in profile (in part b) shows the potential is influenced by the concentration of charge adsorbed at the IHP and provides clarity for Figure 13. The large jump in channel charge is explained through the large potential jump between low and high pH values.

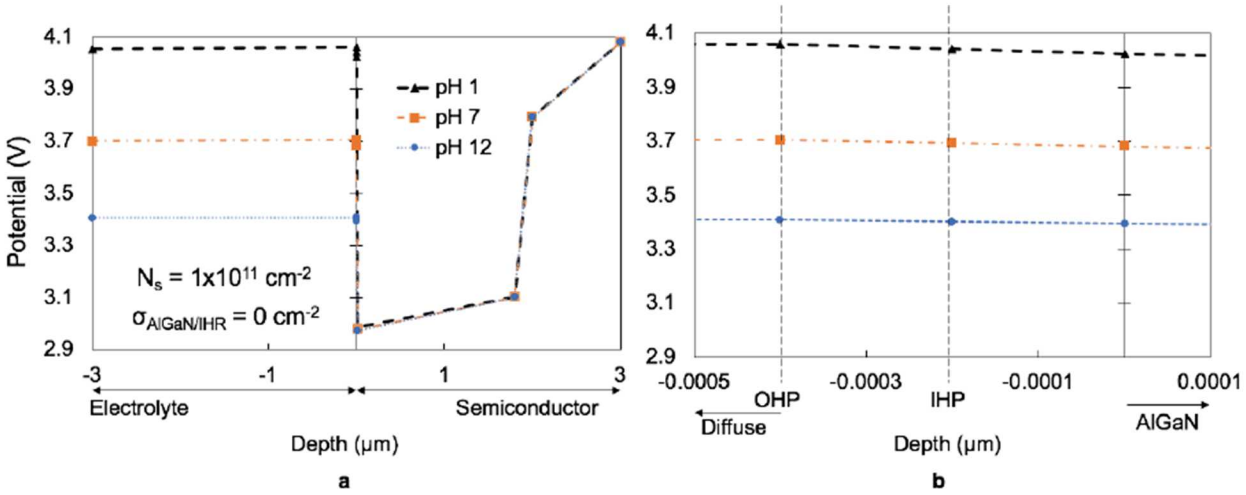

Figure 14. HEMT sensor potential profile for a low value of N_S. (a) The potential profile for the whole system. At -3μm is the bulk of the electrolyte solution and at +3μm is the end of the semiconductor SiC substrate. (b) The potential profile zoomed in to examine the potential profile in the EDL. At -0.0005μm is part of the diffuse region of the EDL and at +0.0001μm is the AlGaN surface of the semiconductor.

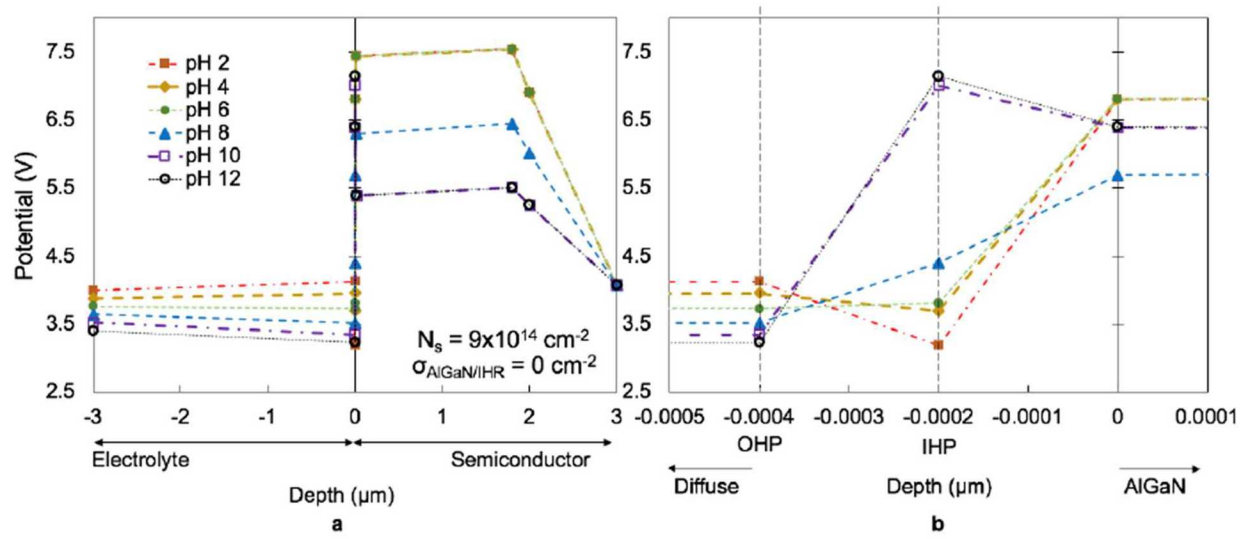

Figure 15. HEMT sensor potential profile for an extreme high value of N_S. (a) The potential profile for the whole system. At -3μm is the bulk of the electrolyte solution and at +3μm is the end of the semiconductor SiC substrate. (b) The potential profile zoomed in to examine the potential profile in the EDL. At -0.0005μm is part of the diffuse region of the EDL and at +0.0001μm is the AlGaN surface of the semiconductor.

To further explain the potential profile in Figure 15, the concentration of charges in each material was examined for N_S equal to 9x10^{14} cm^{-2}. A graphical conclusion for the sum of charge in each area is shown in Figure 16. Part a is a rendering of the HEMT sensor structure simulated with the corresponding AlGaN-GaN HEMT polarization charges. Part b describes the balance of charge in each material for a given pH range. As shown in Figure 6-1, for the pH range of 1 to 5, a large positive charge is adsorbed at the IHP, with a large negative diffuse charge, and large negative channel charge. A separation of positive and negative charge in the AlGaN region is observed. To keep electroneutrality, the AlGaN region becomes two regions of charge, where the top is negative to balance the adsorbed charge and the bottom is positive to balance the 2DEG charge. In the next

pH range, 6 to 8, the adsorbed charge is less in magnitude to switch from positive to negative (SOH_2^+ to SO^-) and the diffuse charge becomes net positive. In the last pH range, 9 to 12, the adsorbed charge is a net negative charge and the AlGaN separation of charge is reversed, where previously it was negative then positive charge and now it is positive and then negative charge (from top down). However, this negative charge in the bottom of the AlGaN, closest to the AlGaN/GaN interface, for this pH range 9-12, is negligible since it is much smaller in magnitude, and results in an overall net positive charge in the AlGaN material. This explains why the 2DEG is not responding to the large adsorbed charge; the AlGaN layer is effectively inverted and masking the 2DEG from the adsorbed charge. The minimum and maximum values of NS for the sensor response is presented in Figure 13. It is clear from this work N_S largely dominates the sensor response of all the parameters explored in this simulation study.

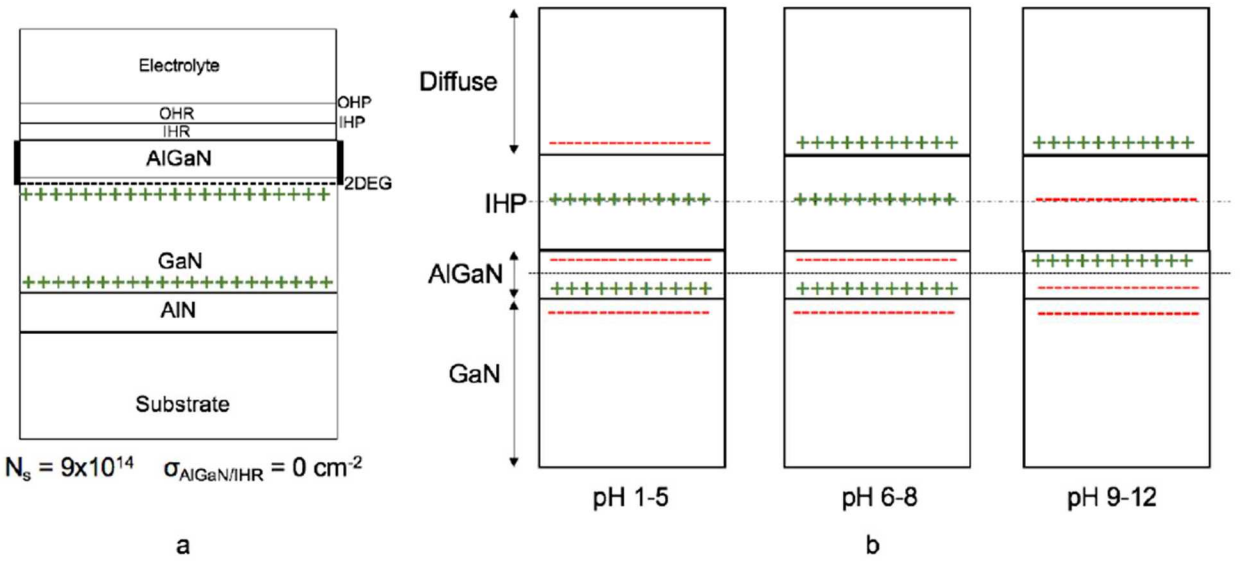

Figure 16. Inverted AlGaN charge in HEMT (a) HEMT sensor structure with strain polarization charges (b) Zoomed in structure for 3 major pH ranges with positive and negative charge concentrations accounted for in each range.

3.2 Equilibrium Rates

Of great interest in sensor response is the effect of equilibrium rate dependence on potential compared to an equilibrium rate as a constant value. The range of N_S was further explored within the bounds previously discussed and the equilibrium rate is with an exponential dependence on potential, presented in Figure 17, is compared with equilibrium rates as a constant value, presented in Figure 18. The magnitude of adsorbed charge concentration plays a significant role in the channel response and is key to tuning the optimum sensitivity of the device. As N_S increases, the adsorbed charge increases, where the 2DEG charge increases as well (except for the inverted charge case discussed previously with N_S equal to 9x1014 cm^{-2}). The N_S was set to a reasonable value, $3x10^{14}$ cm^{-2}, to achieve a sensor response (or a change in the 2DEG charge) and the AlGaN surface charge was set to 0 cm^{-2} (zero charge), where the two methods of equilibrium rates were compared. These results are shown in Figure 19 where the exponential dependence “smooths” the adsorbed charge curve approaching linearity (in part a); yet the 2DEG response (part b) does not follow this trend. The exponential dependence on

potential in the equilibrium rates pushes the response towards being linear, however, the channel charge concentration response with pH does not become linear. Using an equilibrium rate that is exponentially dependent on potential is more realistic than using a constant value [51]. Hence forth the remainder of the results will examine cases only with the equilibrium rate as an exponential dependence on potential.

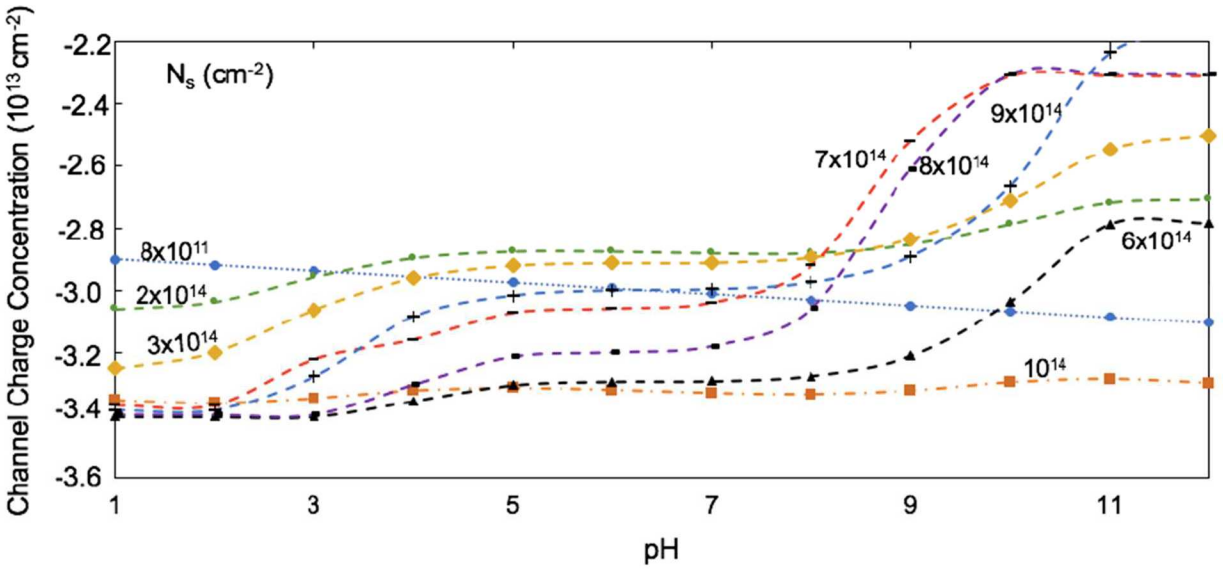

Figure 17. Channel charge concentration with varied available adsorbed charge, N_S, for an equilibrium rate with an exponential dependence on potential. The AlGaN surface charge was kept at zero.

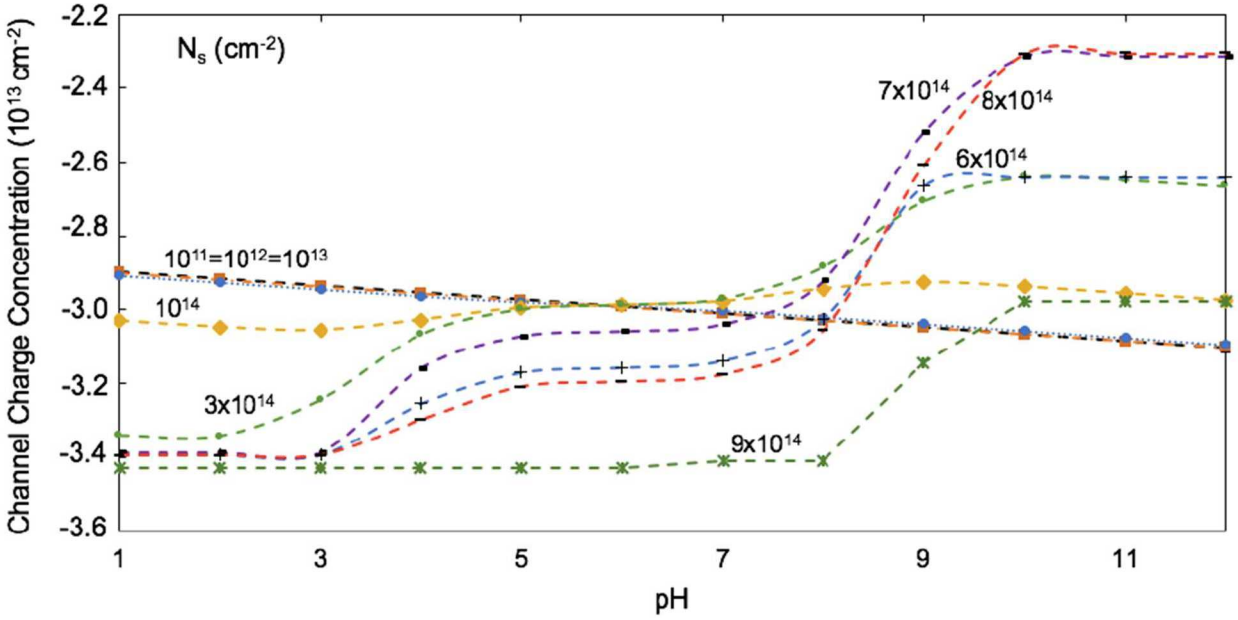

Figure 18. Channel charge concentration with varied available adsorbed charge, N_S, for an equilibrium rate expressed as a constant. The AlGaN surface charge was kept at zero.

For this method of modeling, the equilibrium rates as an exponential dependence on potential, the potential in the bulk electrolyte, OHP, IHP, and AlGaN surface are presented in Figure 20. It is interesting to observe the potential of the bulk electrolyte mirroring the

OHP where the IHP potential mirrors the AlGaN surface potential. This behavior indicates adsorbed charge on the IHP has a direct relationship with the surface of the AlGaN layer. This is expected since the distance between the two interfaces is very small at only 2Å.

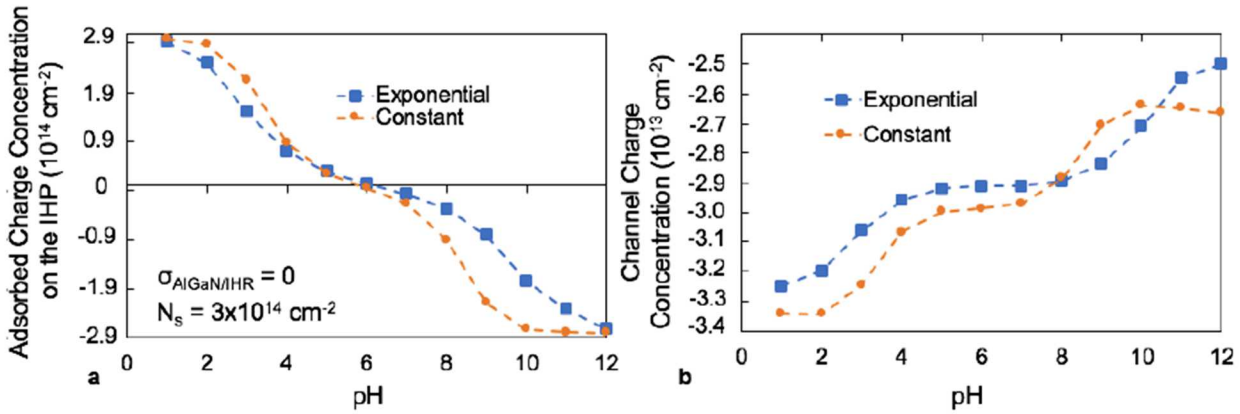

Figure 19. Two methods of implementing equilibrium rates: constant versus exponential dependence on potential. (a) Adsorbed charge concentration on the IHP. (b) Channel charge concentration with respect to pH.

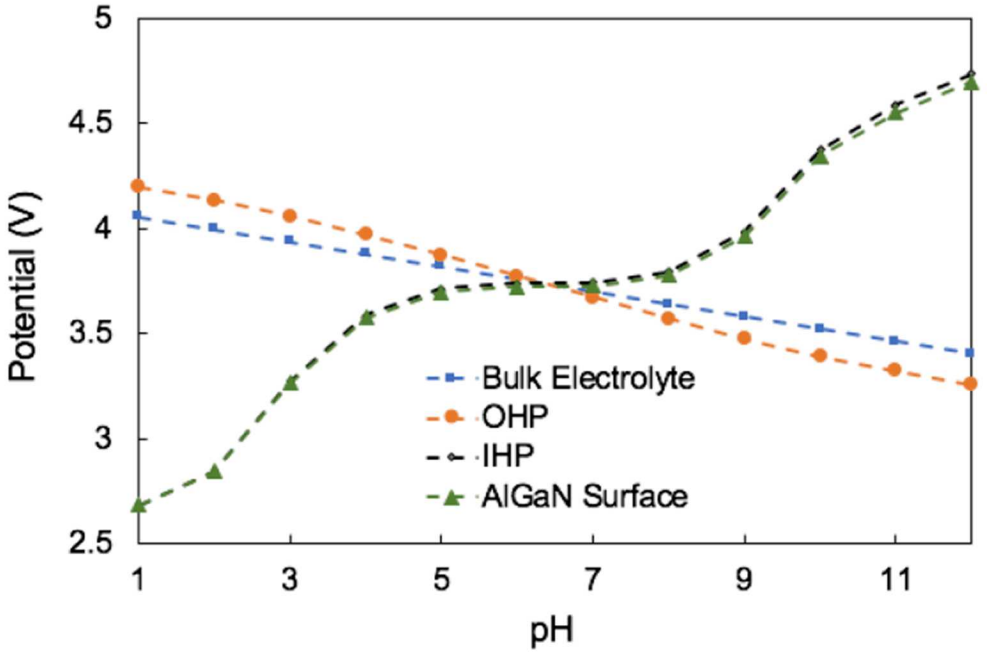

Figure 20. Potential at the edge of the electrolyte (or bulk electrolyte), OHP, IHP, and surface of the AlGaN with respect to pH.

3.3 Passivation Charge

Previous results presented have a surface charge concentration at the top of the AlGaN layer set to 0 cm^{-2}. However, passivating the surface with different charges unintentionally in an experimental environment is inevitable and it is important to understand the effect of different surface charges on the sensor response. The AlGaN surface charge concentration was explored with a reasonable N_S value ($3x10^{14}$ cm^{-2}). The results are shown in Figure 21 and Figure 22. The value of the AlGaN surface charge concentration shifts the magnitude of 2DEG channel charge concentration. As the AlGaN surface charge concentration increases, the 2DEG charge concentration reduces (shifts up

towards zero). Recall that the HEMT total polarization charge below the AlGaN layer equals $+3.26 \times 10^{13}$ cm^{-2}, therefore an AlGaN surface charge of -3.26×10^{13} cm^{-2} would make the HEMT device electrically neutral. Interestingly, a large amount of charge, $+2.26 \times 10^{13}$ cm^{-2}, decreased the sensitivity or the change in 2DEG charge concentration with pH. This was due to a substantial amount of charge in the AlGaN layer which is again masking the 2DEG from responding and compensating for the charge at the surface and prevents a large response from the 2DEG channel. The change in passivation charge does not largely affect the adsorbed charge depicted in Figure 22 part a. In part b, for the extreme pH values (both high and low pHs), the total interface charge concentration is largely dominated by one of the adsorbed charge species; at low pH, the total interface charge is dominated by positive adsorbed charge (negative charge for high pH).

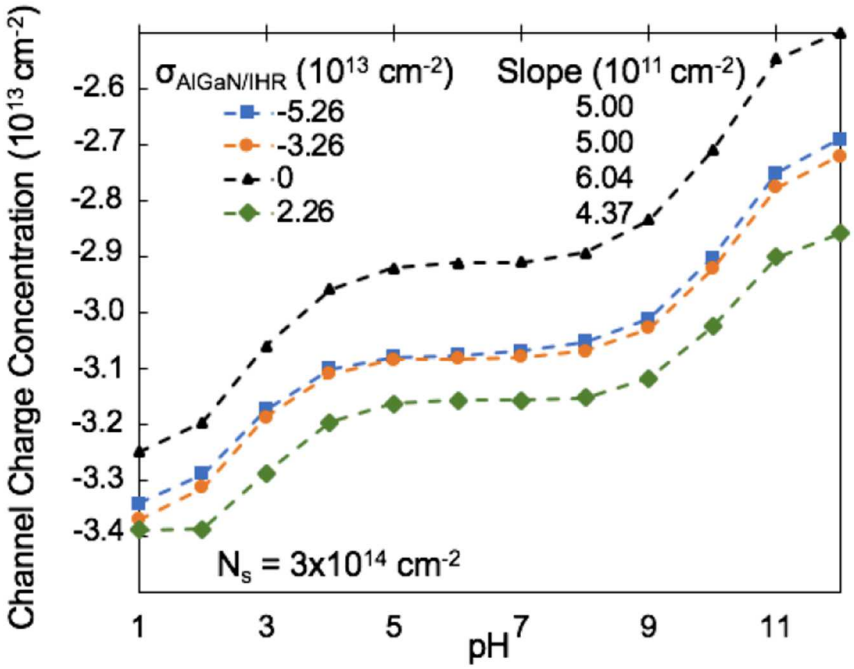

Figure 21. Channel charge concentration for a high N_S value (3×10^{14} cm^{-2}) at varied surface charge concentration on the top of the AlGaN layer.

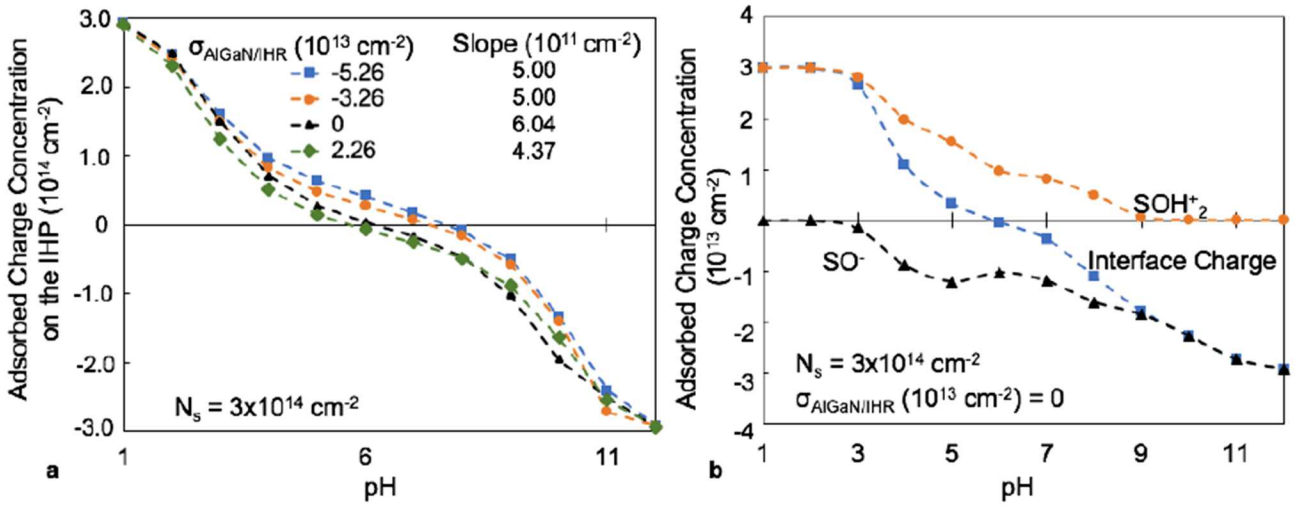

Figure 22. Adsorbed charge concentration for varied AlGaN surface charge concentrations. (a) Adsorbed charge concentration at the IHP with a reasonable N_S value ($3x10^{14}$ cm^{-2}) for varied AlGaN surface charge concentrations. (b) Concentrations for specific adsorbed charges with respect to pH for a given AlGaN surface charge concentration set to 0.

3.4 Linear 2DEG Sensor Response

In this work presented thus far, a linear response for the channel charge with pH is not observed. For a model to be linear, the slope must be constant. With a reasonable N_S value (i.e. N_S equal to $3x10^{14}$ cm^{-2}), the transition region of adsorbed charge from positive to negative, roughly around the pH range of 5 to 8, breaks the constant slope (refer back to Figures 17 through 19). This is due to a large shift in magnitude of adsorbed charge. To make the response more linear for a large N_S value, the transition region needs to be minimized so that this small amount of charge occurs only at one pH instead of 3 or more. It would be desired to have a high N_S value where the 2DEG channel charge concentration can have a larger swinger, however, this sacrifices a linear response.

Another approach to achieving a linear 2DEG response is to cut off the sharp slopes observed at extreme pH values. A narrowed in window of Figure 19 is presented in Figure 23 where a smaller pH range, from 4 to 9, is examined to observe a near-linear 2DEG response. From this narrowed pH range, a linear line is fitted to these points, which is a method reported by experimental results from Huang et al. and Dong et al. [33], [38]. It is worth noting the experimental work from Huang et al. and Dong et al. mirror the same non-linear trend (“S” curve) observed in simulation work presented here.

The concentration of charge for each different region throughout the device/system is examined for each N_S value and is shown in Figure 24 for a high pH value of 11 and a middle pH value of 7. For a large pH value of 11 at higher values of N_S, the AlGaN charge at the bottom (which is closest to the 2DEG), increased in orders of magnitude. This explains the large shift in the 2DEG charge for varied N_S at a large pH value in Figures 17 and 18. At pH of 7, the charge in the AlGaN layer is always negative with N_S and is assisting the 2DEG charge in compensating for adsorbed charge. This is due to the 2DEG charge effectively being capped out or being the largest it can be. In order to maintain electroneutrality, the AlGaN layer compensates for adsorbed charge. The potential profile

was examined for an optimum N_S value of $3x10^{14}$ cm^{-2} and is presented in Figure 25. The potential for pH 6 is roughly flat through the EDL and to the surface of the semiconductor indicating a true equilibrium potential value. The potential of the remaining pHs mirror each other but experience cross over regions as expected with the switch from positive to negative value of adsorbed charge. Due to the observed non-linear response, a consistent sensitivity (or slope) of potential change with pH could not be achieved.

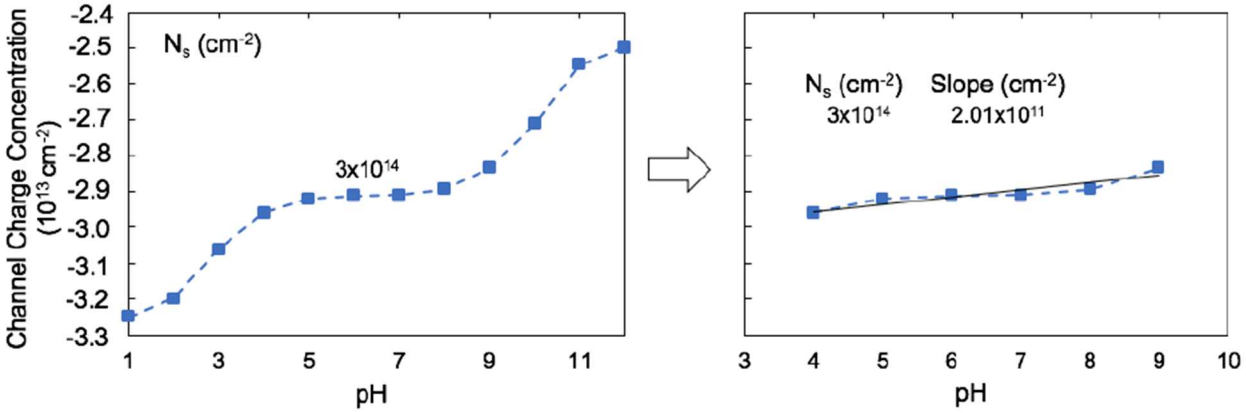

Figure 23. Channel charge concentration versus pH with N_S value $3x10^{14}$ cm^{-2} for AlGaN surface charge of zero. The pH range is narrowed to achieve a near-linear response to compare to reported experimental activities.

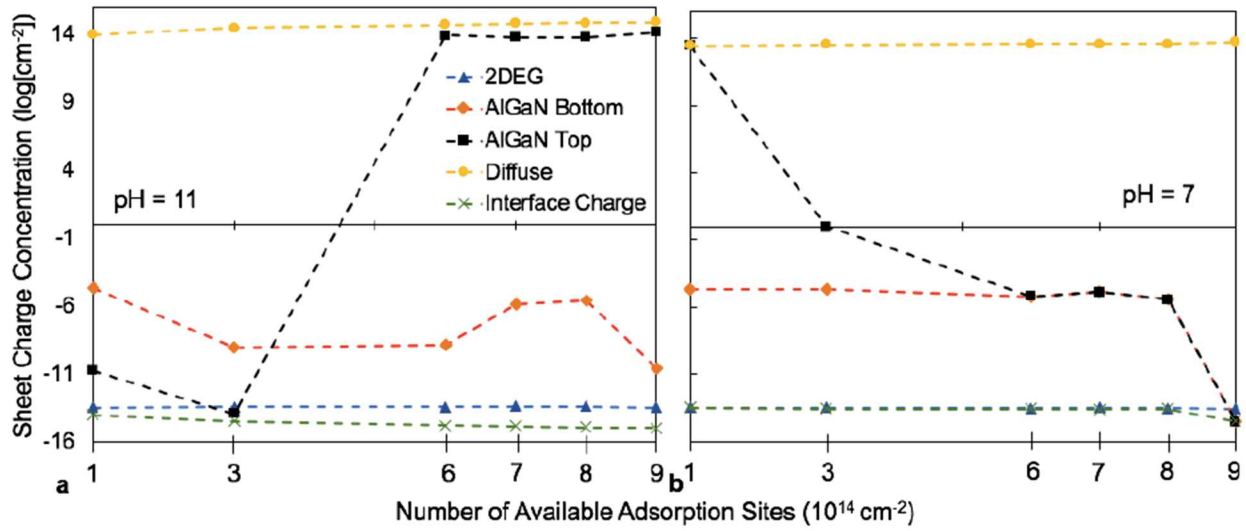

Figure 24. The concentration of charges throughout the device with respect to N_S values for a high pH value of 11 and a middle range pH value of 7.

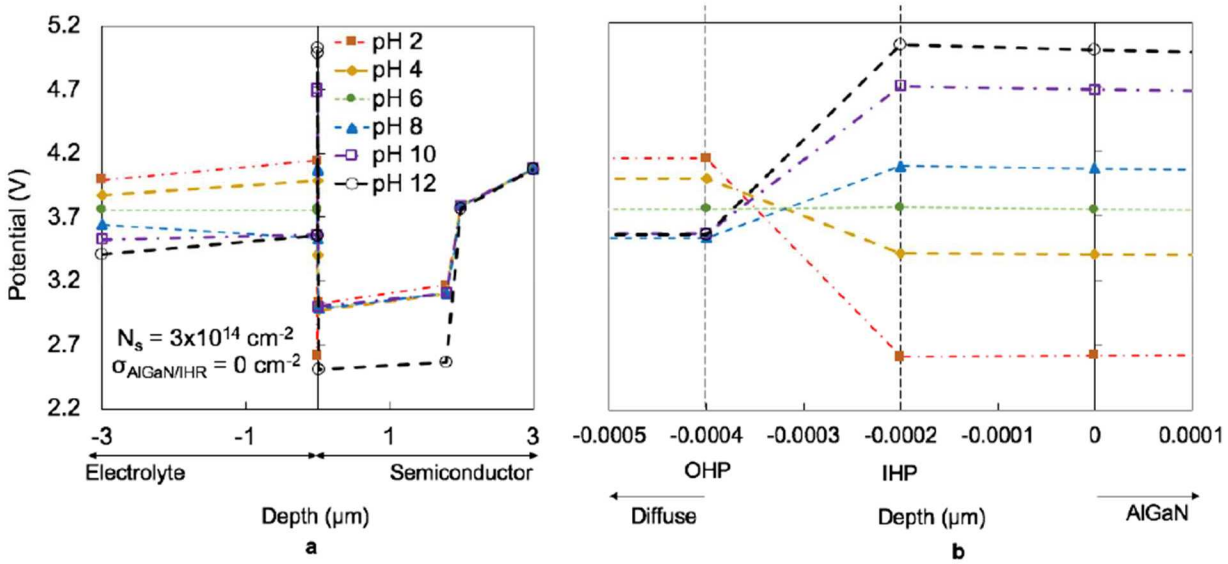

Figure 25. Potential as a function of depth for N_S value of 3x10^{14} cm^{-2}.

3.5 Drain Bias

Lastly, an applied bias was placed onto the back of the AlGaN layer to mimic the effect of a 2-D source to drain bias. The range of applied bias tested was -0.5V to +0.5V. The 0 to +0.5V bias range is reasonable given experimental results [22], [23], [28], [30], [32], [33], [35], [34], [37]–[39], [73]. There were convergence issues for a reasonable N_S value leaving only a small N_S of 10^{11} cm^{-2} to be tested. The sensor response did not change for this case, as expected since the N_S was so small, yet the two methods of equilibrium rate as constant versus exponential dependence on potential were compared. With constant equilibrium rates, little changed and was uninteresting. With exponential dependence on potential in the equilibrium rate, the response changed drastically with applied drain bias. These results are shown in Figure 26. Three pH values were compared (a low value of 1, a middle value of 7, and a high value of 12) where the true adsorption behavior of these pHs were only observed at 0V applied bias. Once a bias of + or -0.1V was applied, the reaction was forced to an extreme behavior of the adsorption model. This is reasonable if we recall pH 1 has a high potential value and pH 12 has a low potential (recall Nernst behavior), where at a low pH (high potential) the adsorbed charge is largely positive and negative for high pH. If we compare the -0.5V extreme to the pH 12, it is rational that the adsorption model would be an extreme value of negatively adsorbed charge. The same is true for a +0.5V bias to compare to pH 1 with a large positive adsorbed charge. On either side of zero bias, the smallest applied bias of 0.1V is large enough to swing the adsorption model to its extreme and fully adsorbed case, since the equilibrium rate is exponentially dependent on potential.

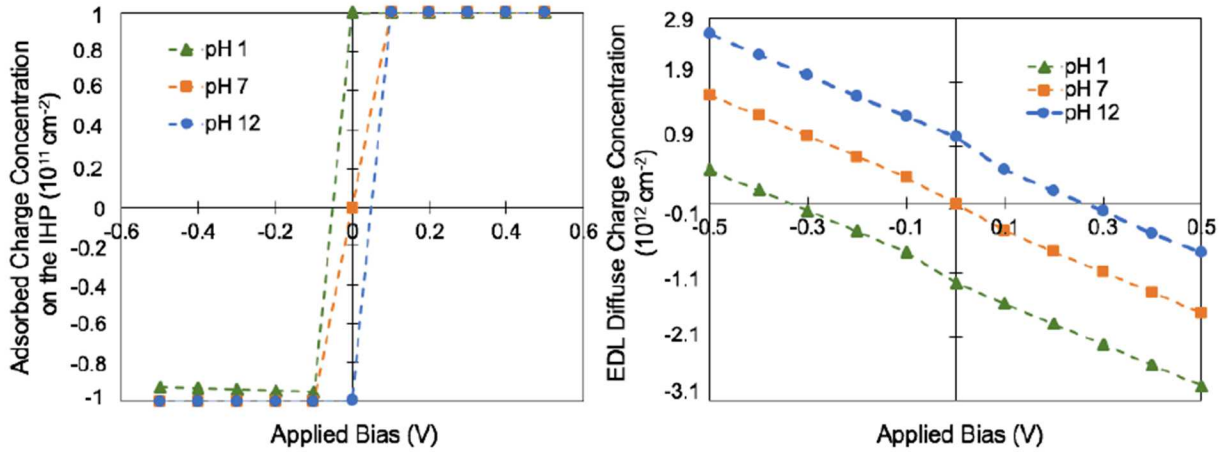

Figure 26. Applied Bias with Equilibrium Rate Potential Exponential Dependence. (a) Adsorbed charge concentration on the IHP as a function of applied bias on the AlGaN backside with equilibrium rate as an exponential dependence on potential for varied pH values.

Since only a small N_S value could be simulated, the sensor response was not achieved and the channel charge did not change with this drastic charge in the adsorption model. However, it is expected with larger and more reasonable N_S values, where the sensor response occurs, this effect would drastically change the sensor response. In a previous study without the EDL but in 2-D, the interface charge was found to vary spatially. At a given pH and applied drain bias, the interface charge would be positive on one side of the channel and have a gradual shift to negative on the other side of the channel [49]. This is expected to be a result of the applied drain bias having an effect on the adsorption model. However this study did not have an exponential dependence on potential in the equilibrium rate. Given this drain bias dependence is spacial, if it were to be combined with an exponential dependence on potential in the equilibrium rate, the interface charge would vary significantly. Based on this first approximation, the source to drain bias for a 2-D model with exponential equilibrium rate dependence on bias would play a significant role in the channel charge. It is expected that, instead of a gradual shift from positive to negative observed in previous work [49], a dramatic shift from positive to negative interface charge would occur and this could lead to significant reliability issues in the sensor response. Overall the sensor response was observed as largely dependent on N_S (compared to the variables studied here: AlGaN surface charge and equilibrium rate).

Comparing Simulation work with Experimental Results

While most experimental work reports potential sensitivity, as mV/pH, to compare with Steinhoff et al. [23] and to compare to the maximum Nernst theoretical value (-59 mV/pH), a few papers report sensitivity as a change in the channel current. Reporting the sensitivity as a change in current is more useful than a change in potential since the sensor can more readily measure a change in current as it outputs a current value. The tables below provide a synopsis of these current measured sensitivities and how our simulation results compare to them.

The simulated sensitivities are expressed by equation 37 and calculated from simulated 2DEG charge concentration with the equilibrium rate as an exponential dependence on

potential where a maximum sensitivity was achieved with the AlGaN surface charge concentration was set to 0 cm^{-2} and the N_S set to $3x10^{14}$ cm^{-2}. The 2DEG charge concentration is noted as Q, the mobility of the 2DEG is noted as μ, L_{cm} is the channel gate length in cm, W_{cm} is the channel gate width in cm, and V_{DS} is the applied drain bias. The 2DEG charge concentration was taken from these 1-D simulations and the remaining parameters were matched with its respective experiment to compare sensitivity values. The current is measured as amperes and can be written, for a linear region of operation, as:

$$I\,(A) = \frac{Q\mu V_{DS} W_{cm}}{L_{cm}} \qquad 37$$

Author	Oxide	pH Range	Gate Dimensions	Mobility (cm^2/Vs)	Drain Bias (V)
Kang et al. [9], [39]	Native oxide and Sc_2O_3	3 to 10	2 x 150 μm^2	980	0.25
Abidin et al. [37]	Native oxide	1.7 to 11.9	40 x 490 μm^2	1860	0.5
Brazzini et al. [35]	Native oxide	4 to 10	1.2 x 0.5 mm^2	400	0.2
*Dong et al. [38]	Native oxide	4 to 8	13 x 250 μm^2 175 x 250 μm^2 175 x 50 μm^2	1730	1.5
Huang et al. [33]	Native oxide	P: 7 to 8 A: 4 to 10	15 x 15 μm^2	750 to 1150	0.25

*Table 1. Summary of Experimental Work. (*The exposed gate length was 10um for all source to drain dimensions listed.) P is the peak value and A is the average value.*

Author	Experimental Sensitivity	FLOODS Sensitivity
Kang et al. [9], [39]	Native oxide: 70 μA Sc_2O_3: 37 μA/pH	0.588 mA/pH
Abidin et al. [37]	1.9 mA/pH or 3.88 mA/mm-pH	1.825 mA/pH or 3.725 mA/mm-pH
Brazzini et al. [35]	P: 40 μA/pH A: 2.83 μA/pH	1.074 μA/pH
*Dong et al. [38]	1.35 mA/pH 21.29 μA/pH 7.08 μA/pH	1.599 mA/pH 23.75 μA/pH 4.75 μA/pH
Huang et al. [33]	P: 2.24 mA/mm-pH A: 0.923 mA/mm-pH	0.617 mA/mm-pH

Table 2. Summary of Experimental Sensitivity with simulated FLOODS Sensitivity. (P is the peak value and A is the average value). FLOODS pH range of 4 to 9 with equilibrium rates with the exponential dependence on potential was used for the sensitivity calculation.

Overall FLOODS simulation sensitivities were within reasonable percent error of experimental work except for the work reported by Kang et al. [9], [39]. Since the surface

charge of the AlGaN layer accompanied with the presence and thickness of an oxide layer is not discussed in detail for most of the experimental work, including work reported from Kang et al., it is likely these factors are the root of any discrepancies. Without further information from these studies, an exact justification or investigation cannot be made. It is worth noting work from Abidin et al. [37] reported sensitivities at a large drain bias where it is assumed this sensor was operating in a saturation region. The charge in the channel is largely inverted and pinched-off where the current is reduced by a factor of 2. Our simulated results were halved to reflect this change from linear to saturation region of the transistor operation. It is also worth noting the work from Dong et al. [38] had a varied gate length (distance between drain and source contacts) but the exposed gate length remained the same. In this case, the drain bias is different for the region of the exposed surface when the distance between the drain and source contacts is increased. We approximated a reasonable drain bias voltage, based on their figures, to compare with our simulated sensitivity.

Future Work

The HEMT sensor with the EDL and specific adsorption models thus far could only be simulated in one-dimension in FLOODS due to convergence issues associated with tuning and solving a solution variable with an exponential dependence on potential. To expand this model to 2-D will require mathematical correction in the exponential function to improve convergence. 2-D models should be explored further to combine the electrochemical reaction rate dependence on potential to test the source to drain current effect. The drain to source potential variation is expected to contribute voltage to the exponential dependence on potential of the equilibrium rates. The reaction, and therefore the HEMT sensor response, could vary exponentially along the direction of the gate length, or conducting channel.

Another idea for further work is to explore different oxides with varied thicknesses and quality. Since the thickness of oxides can vary in the fabrication process (native oxide versus thermally-grown versus deposited oxide), a large oxide thickness is expected to cause a decrease in the sensitivity as the electrostatic force between the 2DEG charge and the adsorbed charge is decreased. A study of the limitations for oxide thicknesses of this nature should be explored. The quality of oxides are known to differ with varied fabrication methods and it is expected that the quality of oxides can also have an effect on sensitivity [9], [39]. If a poor oxide is used (one with less oxygen available for hydrogen to bond with) it can hinder the adsorption reaction at the surface and can cause a degradation in the 2DEG response. Kang et al. compares two oxides, a high-quality oxide deposited versus a native oxide [9], [39]. While the deposited oxide was a higher quality and lead to higher stability, the thickness of the oxide is also much larger for deposited oxide than a native oxide and the magnitude of the sensitivity was lower. Hence a simulation study of these two mechanisms to evaluate the limitations between the two can produce an optimum sensitivity.

Combining knowledge of the oxide effects on the sensor response with varied electrolyte solutions of varied molecule size and dipole moment can lead to a better understanding of the sensor response. There is sufficient experimental work studying the effect of different supporting electrolytes and the selectivity of the GaN to anions [28]–[31], [36]. In FLOODS simulations, the charges in the electrolyte are treated as electrons and holes, where the size does not play a role in the diffusion. It is expected the size and orientation of the molecules will affect the reaction rate of the adsorbed charge and this would vary with different supporting electrolytes. The TLM implemented by Anvari et al. [44] analyzes the selectivity of the surface to pH, the ionic strength, and ionic types, and are all explained by the equilibrium rates since the TLM takes water molecule effects into account with charge to be adsorbed on the oxide surface. This method seems more accurate to model the reaction at the oxide surface and is complex. If it could be implemented in FLOODS and compared with the simpler EDL with specific adsorption used in this project, it could be better understood if the TLM complex model is needed or if our EDL model will suffice. Based on experimental results, the EDL model appears more accurate, however, the TLM discusses dipole moment and molecule size to make the reaction more complex and understanding this effect on the sensor response can be useful. Furthermore, this model should be combined with a study of the various oxides (grown versus deposited, thickness, quality, etc) to better understand how to increase the sensor response.

Lastly, only the equilibrium rate is studied since only steady-state cases are explored, which is a great first step in simulating this sensor. Transient simulations should be built to understand the balance between the forward and reverse reaction rates. These transient simulations can be integrated with an understanding of various oxides. In Kang et al. [39] a native oxide was compared with deposited scandium oxide, where resolution was compared and other experimental work also present sensor current as a function of time [1], [9], [29], [32], [35], [38], [73]. Simulating these effects with transient analysis can lead to a better understanding of the 2DEG response to optimize the GaN-based HEMT pH sensor, ultimately building a more complete model of this sensor.

References

[1] B. H. Chu *et al.*, “Wireless Detection System for Glucose and pH Sensing in Exhaled Breath Condensate Using AlGaN/GaN High Electron Mobility Transistors,” *IEEE Sens. J.*, vol. 10, no. 1, pp. 64–70, Jan. 2010.

[2] B. S. Kramer, M. L. Brown, P. C. Prorok, and J. K. Gohagan, “Prostate cancer screening: what we know and what we need to know,” *Ann. Intern. Med.*, vol. 119, no. 9, pp. 914–923, 1993.

[3] T. Kullmann *et al.*, “Exhaled breath condensate pH standardised for CO2 partial pressure,” *Eur. Respir. J.*, vol. 29, no. 3, pp. 496–501, Mar. 2007.

[4] R. F. Machado *et al.*, “Detection of Lung Cancer by Sensor Array Analyses of Exhaled Breath,” *Am. J. Respir. Crit. Care Med.*, vol. 171, no. 11, pp. 1286–1291, Jun. 2005.

[5] I. Horváth, J. Hunt, and P. J. Barnes, “Exhaled breath condensate: methodological recommendations and unresolved questions,” *Eur. Respir. J.*, vol. 26, no. 3, pp. 523–548, Sep. 2005.

[6] J. Vaughan *et al.*, “Exhaled breath condensate pH is a robust and reproducible assay of airway acidity,” *Eur. Respir. J.*, vol. 22, no. 6, pp. 889–894, Dec. 2003.

[7] T. Kullmann, I. Barta, B. Antus, M. Valyon, and I. Horvath, “Environmental temperature and relative humidity influence exhaled breath condensate pH,” *Eur. Respir. J.*, vol. 31, no. 2, pp. 474–475, Feb. 2008.
[8] K. Namjou, C. Roller, and P. McCann, “The Breathmeter - A new laser device to analyze your health,” *IEEE Circuits Devices Mag.*, vol. 22, no. 5, pp. 22–28, Sep. 2006.
[9] B. S. Kang *et al.*, “Role of Gate Oxide in AlGaN/GaN High-Electron-Mobility Transistor pH Sensors,” *J. Electron. Mater.*, vol. 37, no. 5, pp. 550–553, May 2008.
[10] K. H. Chen *et al.*, “c-erbB-2 sensing using AlGaN⁄GaN high electron mobility transistors for breast cancer detection,” *Appl Phys Lett*, p. 4.
[11] B. S. Kang *et al.*, “Prostate specific antigen detection using AlGaN⁄GaN high electron mobility transistors,” *Appl. Phys. Lett.*, vol. 91, no. 11, p. 112106, Sep. 2007.
[12] H. T. Wang *et al.*, “Electrical detection of kidney injury molecule-1 with AlGaN⁄GaN high electron mobility transistors,” *Appl. Phys. Lett.*, vol. 91, no. 22, p. 222101, Nov. 2007.
[13] J. F. Hunt *et al.*, “Endogenous Airway Acidification: Implications for Asthma Pathophysiology,” *Am. J. Respir. Crit. Care Med.*, vol. 161, no. 3, pp. 694–699, Mar. 2000.
[14] S. J. Pearton *et al.*, “GaN-based diodes and transistors for chemical, gas, biological and pressure sensing,” *J. Phys. Condens. Matter*, vol. 16, no. 29, pp. R961–R994, Jul. 2004.
[15] J. Schalwig, G. Muller, O. Ambacher, and M. Stutzmann, “Group-III-Nitride Based Gas Sensing Devices,” *Phys. Status Solidi A*, vol. 185, no. 1, pp. 39–45, May 2001.
[16] M. Eickhoff *et al.*, “Electronics and sensors based on pyroelectric AlGaN/GaN heterostructures - Part B: Sensor applications,” *Phys. Status Solidi C*, vol. 0, no. 6, pp. 1908–1918, Sep. 2003.
[17] M. Eickhoff, R. Neuberger, G. Steinhoff, O. Ambacher, G. Muller, and M. Stutzmann, “Wetting Behaviour of GaN Surfaces with Ga- or N-Face Polarity,” *Phys. Status Solidi B*, vol. 228, no. 2, pp. 519–522, Nov. 2001.
[18] J. Kim, B. P. Gila, G. Y. Chung, C. R. Abernathy, S. J. Pearton, and F. Ren, “Hydrogen-sensitive GaN Schottky diodes,” *Solid-State Electron.*, vol. 47, no. 6, pp. 1069–1073, Jun. 2003.
[19] J. Kim, F. Ren, B. P. Gila, C. R. Abernathy, and S. J. Pearton, “Reversible barrier height changes in hydrogen-sensitive Pd/GaN and Pt/GaN diodes,” *Appl. Phys. Lett.*, vol. 82, no. 5, pp. 739–741, Feb. 2003.
[20] J. Kim, B. P. Gila, C. R. Abernathy, G. Y. Chung, F. Ren, and S. J. Pearton, “Comparison of Pt/GaN and Pt/4H-SiC gas sensors,” *Solid-State Electron.*, vol. 47, no. 9, pp. 1487–1490, Sep. 2003.
[21] O. Ambacher *et al.*, “Electronics and sensors based on pyroelectric AlGaN/GaN heterostructures,” *Phys. Status Solidi C*, vol. 0, no. 6, pp. 1878–1907, Sep. 2003.
[22] B. S. Kang *et al.*, “Effect of external strain on the conductivity of AlGaN/GaN high-electron-mobility transistors,” *Appl. Phys. Lett.*, vol. 83, no. 23, pp. 4845–4847, Dec. 2003.
[23] G. Steinhoff, M. Hermann, W. J. Schaff, L. F. Eastman, M. Stutzmann, and M. Eickhoff, “pH response of GaN surfaces and its application for pH-sensitive field-effect transistors,” *Appl. Phys. Lett.*, vol. 83, no. 1, pp. 177–179, Jul. 2003.
[24] P. Bergveld, “Development of an Ion-Sensitive Solid-State Device for Neurophysiological Measurements,” *IEEE Trans. Biomed. Eng.*, vol. BME-17, no. 1, pp. 70–71, Jan. 1970.
[25] P. Bergveld, “Development, Operation, and Application of the Ion-Sensitive Field-Effect Transistor as a Tool for Electrophysiology,” *IEEE Trans. Biomed. Eng.*, vol. BME-19, no. 5, pp. 342–351, Sep. 1972.
[26] J. Schalwig, G. Muller, M. Eickhoff, O. Ambacher, and M. Stutzmann, “Gas sensitive GaN/AlGaN-heterostructures,” *Sens. Actuators B Chem.*, vol. 87, no. 3, pp. 425–430, Dec. 2002.
[27] M. Stutzmann *et al.*, “GaN-based heterostructures for sensor applications,” *Diam. Relat. Mater.*, vol. 11, no. 3–6, pp. 886–891, Mar. 2002.

[28] R. Mehandru *et al.*, “AlGaN/GaN HEMT based liquid sensors,” *Solid-State Electron.*, vol. 48, no. 2, pp. 351–353, Feb. 2004.
[29] R. Neuberger, G. M□ller, O. Ambacher, and M. Stutzmann, “High-Electron-Mobility AlGaN/GaN Transistors (HEMTs) for Fluid Monitoring Applications,” *Phys. Status Solidi A*, vol. 185, no. 1, pp. 85–89, May 2001.
[30] Y. Alifragis, A. Volosirakis, N. A. Chaniotakis, G. Konstantinidis, E. Iliopoulos, and A. Georgakilas, “AlGaN/GaN high electron mobility transistor sensor sensitive to ammonium ions,” *Phys. Status Solidi A*, vol. 204, no. 6, pp. 2059–2063, Jun. 2007.
[31] N. A. Chaniotakis, Y. Alifragis, A. Georgakilas, and G. Konstantinidis, “GaN-based anion selective sensor: Probing the origin of the induced electrochemical potential,” *Appl. Phys. Lett.*, vol. 86, no. 16, p. 164103, Apr. 2005.
[32] T. Kokawa, T. Sato, H. Hasegawa, and T. Hashizume, “Liquid-phase sensors using open-gate AlGaN/GaN high electron mobility transistor structure,” *J. Vac. Sci. Technol. B Microelectron. Nanometer Struct.*, vol. 24, no. 4, p. 1972, 2006.
[33] H.-S. Huang, C.-W. Lin, and H.-C. Chiu, “High Sensitivity pH Sensor Using AlXGa1-XN/GaN HEMT Heterostructure Design,” p. 4.
[34] K. Niigata, K. Narano, Y. Maeda, and J.-P. Ao, “Temperature dependence of sensing characteristics of a pH sensor fabricated on AlGaN/GaN heterostructure,” *Jpn. J. Appl. Phys.*, vol. 53, no. 11S, p. 11RD01, Nov. 2014.
[35] T. Brazzini, A. Bengoechea-Encabo, M. A. Sánchez-García, and F. Calle, “Investigation of AlInN barrier ISFET structures with GaN capping for pH detection,” *Sens. Actuators B Chem.*, vol. 176, pp. 704–707, Jan. 2013.
[36] A. Podolska *et al.*, “Ion versus pH sensitivity of ungated AlGaN/GaN heterostructure-based devices,” *Appl. Phys. Lett.*, vol. 97, no. 1, p. 012108, Jul. 2010.
[37] M. S. Z. Abidin, A. M. Hashim, M. E. Sharifabad, S. F. A. Rahman, and T. Sadoh, “Open-Gated pH Sensor Fabricated on an Undoped-AlGaN/GaN HEMT Structure,” *Sensors*, vol. 11, no. 3, pp. 3067–3077, Mar. 2011.
[38] Y. Dong *et al.*, “AlGaN/GaN heterostructure pH sensor with multi-sensing segments,” *Sens. Actuators B Chem.*, vol. 260, pp. 134–139, May 2018.
[39] B. S. Kang *et al.*, “pH sensor using AlGaN/GaN high electron mobility transistors with Sc2O3 in the gate region,” *Appl. Phys. Lett.*, vol. 91, no. 1, p. 012110, Jul. 2007.
[40] D. Yates, S. Levine, and T. Healy, “Site-bindingModel of the Electrical Double Layer at the Oxide/Water Iiiterface,” *J Chem Soc Faraday Trans 1*, no. 70, pp. 1807–1818, 1974.
[41] S. Levine and A. L. Smith, “Theory of the differential capacity of the oxide/aqueous electrolyte interface,” *Discuss. Faraday Soc.*, vol. 52, p. 290, 1971.
[42] M. Bayer, C. Uhl, and P. Vogl, “Theoretical study of electrolyte gate AlGaN/GaN field effect transistors,” *J. Appl. Phys.*, vol. 97, no. 3, p. 033703, Feb. 2005.
[43] P. Bergveld and A. Sibbald, *Comprehensive Analytical Chemistry: analytical and biomedical applications of ion-selective fieldeffect transistors*, vol. 23. Amsterdam: Elsevier, 1988.
[44] R. Anvari, D. Spagnoli, G. A. Umana-Membreno, G. Parish, and B. Nener, “Theoretical study of the influence of surface effects on GaN-based chemical sensors,” *Appl. Surf. Sci.*, vol. 452, pp. 75–86, Sep. 2018.
[45] N. Sahai and D. A. Sverjensky, “Evaluation of internally consistent parameters for the triple-layer model by the systematic analysis of oxide surface titration data,” *Geochim. Cosmochim. Acta*, vol. 61, no. 14, pp. 2801–2826, Jul. 1997.
[46] D. A. Sverjensky and K. Fukushi, “Anion Adsorption on Oxide Surfaces: Inclusion of the Water Dipole in Modeling the Electrostatics of Ligand Exchange,” *Environ. Sci. Technol.*, vol. 40, no. 1, pp. 263–271, Jan. 2006.
[47] A. Das *et al.*, “GaN Thin Film Based Light Addressable Potentiometric Sensor for pH Sensing Application,” *Appl. Phys. Express*, vol. 6, no. 3, p. 036601, Mar. 2013.

[48] G. Steinhoff, O. Purrucker, M. Tanaka, M. Stutzmann, and M. Eickhoff, “AlxGa1–xN—A New Material System for Biosensors,” *Adv. Funct. Mater.*, vol. 13, no. 11, pp. 841–846, Nov. 2003.
[49] M. Sciullo, M. Choudhury, E. Patrick, and M. E. Law, “Optimization of GaN-Based HEMTs for Chemical Sensing: A Simulation Study,” *ECS Trans.*, vol. 75, no. 16, pp. 259–264, Aug. 2016.
[50] E. Patrick, M. Choudhury, and M. E. Law, “Simulation of the pH Sensing Capability of an Open-Gate GaN-Based Transistor,” *ECS Trans.*, vol. 69, no. 13, pp. 15–23, Oct. 2015.
[51] M. E. Orazem, “Mathematical modeling and optimization of liquid-junction photovoltaic cells,” University of California, Berkeley, 1993.
[52] M. E. Orazem and J. Newman, “Photoelectrochemical devices for solar energy conversion,” in *Modern Aspects of Electrochemistry*, Springer, 1986, pp. 61–112.
[53] M. E. Orazem and J. Newman, “Mathematical Modeling of Liquid-Junction Photovoltaic Cells,” *J Electrochem Soc*, p. 6, 1984.
[54] M. E. Orazem, J. Newman, M. E. Orazem, and J. Newman, “Mathematical Modeling of Liquid-Junction Photovoltaic Cells,” *J Electrochem Soc*, p. 9, 1984.
[55] D. C. Grahame, “The Electrical Double Layer and the Theory of Electrocapillarity.,” *Chem. Rev.*, vol. 41, no. 3, pp. 441–501, Dec. 1947.
[56] L. Guldbrand, B. Jönsson, H. Wennerström, and P. Linse, “Electrical double layer forces. A Monte Carlo study,” *J. Chem. Phys.*, vol. 80, no. 5, pp. 2221–2228, Mar. 1984.
[57] D. Boda, K.-Y. Chan, and D. Henderson, “Monte Carlo simulation of an ion-dipole mixture as a model of an electrical double layer,” *J. Chem. Phys.*, vol. 109, no. 17, pp. 7362–7371, Nov. 1998.
[58] D. Henderson and D. Boda, “Insights from theory and simulation on the electrical double layer,” *Phys. Chem. Chem. Phys.*, vol. 11, no. 20, p. 3822, 2009.
[59] M. Scaramuzza, A. Ferrario, E. Pasqualotto, and A. De Toni, “Development of an Electrode/Electrolyte Interface Model Based on Pseudo-Distributed Elements Combining COMSOL, MATLAB and HSPICE,” *Procedia Chem.*, vol. 6, pp. 69–78, 2012.
[60] S.-L. Wu, M. E. Orazem, B. Tribollet, and V. Vivier, “The Influence of Coupled Faradaic and Charging Currents on Impedance Spectroscopy,” *Electrochimica Acta*, vol. 131, pp. 3–12, Jun. 2014.
[61] S.-L. Wu, M. E. Orazem, B. Tribollet, and V. Vivier, “The impedance response of rotating disk electrodes,” *J. Electroanal. Chem.*, vol. 737, pp. 11–22, Jan. 2015.
[62] M. E. Law and S. M. Cea, “Continuum based modeling of silicon integrated circuit processing: An object oriented approach,” *Comput. Mater. Sci.*, vol. 12, no. 4, pp. 289–308, Nov. 1998.
[63] D. J. Cummings, M. E. Law, S. Cea, and T. Linton, “Comparison of discretization methods for device simulation,” in *SISPAD International Conference on Simulation of Semiconductor Processes and Devices*, 2009, pp. 1–4.
[64] M. E. Law, M. Griglione, E. Patrick, N. Rowsey, and D. Horton, “Reliability Simulation,” in *Materials and Reliability Handbook for Semiconductor Optical and Electron Devices*, New York, NY: Springer, 2012, pp. 515–544.
[65] D. C. Grahame, “Properties of the Electrical Double Layer at a Mercury Surface. I. Methods of Measurement and Interpretation of Results,” *J. Am. Chem. Soc.*, vol. 63, no. 5, pp. 1207–1215, May 1941.
[66] A. J. Bard and L. R. Faulkner, *Electrochmeical methods: fundamentals and applications*, 2nd ed. New York, NY: John Wiley & Sons Inc., 2001.
[67] J. Newman and K. E. Thomas-Alyea, *Electrochemical Systems*, 3rd ed. Hoboken, New Jersey: John Wiley & Sons Inc., 2004.
[68] O. Stern, “The theory of the electrolytic double-layer,” *Z Elektrochem*, vol. 30, no. 50, pp. 1014–1020, 1924.

[69] O. Ambacher *et al.*, “Two-dimensional electron gases induced by spontaneous and piezoelectric polarization charges in N- and Ga-face AlGaN/GaN heterostructures,” *J. Appl. Phys.*, vol. 85, no. 6, pp. 3222–3233, Mar. 1999.
[70] U. K. Mishra, P. Parikh, and Yi-Feng Wu, “AlGaN/GaN HEMTs-an overview of device operation and applications,” *Proc. IEEE*, vol. 90, no. 6, pp. 1022–1031, Jun. 2002.
[71] M. Farahmand *et al.*, “Monte Carlo simulation of electron transport in the III-nitride wurtzite phase materials system: binaries and ternaries,” *IEEE Trans. Electron Devices*, vol. 48, no. 3, pp. 535–542, Mar. 2001.
[72] M. E. Levinshtein, S. L. Rumyantsev, and M. S. Shur, *Properties of Advanced Semiconductor Materials: GaN, AlN, InN, BN, SiC, SiGe*. Canada: John Wiley & Sons Inc., 2001.
[73] J.-Y. Fang, C.-P. Hsu, Y.-W. Kang, K. C. Fang, F. Ren, and Y.-L. Wang, “Investigation of the Current Stability of AlGaN/GaN High Electron Mobility Transistors in Various Liquid/Solid Interface on the Gate Area,” *ECS Trans.*, vol. 58, no. 8, pp. 3–7, Aug. 2013.